



**HAL**  
open science

**Anatomy of the AGN in NGC 5548. VIII.  
XMM-Newton's EPIC detailed view of an unexpected  
variable multilayer absorber**

M. Cappi, B. de Marco, G. Ponti, F. Ursini, P. -O. Petrucci, S. Bianchi, J. S.  
Kaastra, G. A. Kriss, M. Mehdipour, M. Whewell, et al.

► **To cite this version:**

M. Cappi, B. de Marco, G. Ponti, F. Ursini, P. -O. Petrucci, et al.. Anatomy of the AGN in NGC 5548. VIII. XMM-Newton's EPIC detailed view of an unexpected variable multilayer absorber. *Astronomy and Astrophysics - A&A*, 2016, 592, 10.1051/0004-6361/201628464 . insu-03691534

**HAL Id: insu-03691534**

**<https://insu.hal.science/insu-03691534>**

Submitted on 9 Jun 2022

**HAL** is a multi-disciplinary open access archive for the deposit and dissemination of scientific research documents, whether they are published or not. The documents may come from teaching and research institutions in France or abroad, or from public or private research centers.

L'archive ouverte pluridisciplinaire **HAL**, est destinée au dépôt et à la diffusion de documents scientifiques de niveau recherche, publiés ou non, émanant des établissements d'enseignement et de recherche français ou étrangers, des laboratoires publics ou privés.

# Anatomy of the AGN in NGC 5548

## VIII. *XMM-Newton*'s EPIC detailed view of an unexpected variable multilayer absorber

M. Cappi<sup>1</sup>, B. De Marco<sup>2</sup>, G. Ponti<sup>2, 1</sup>, F. Ursini<sup>3, 4</sup>, P.-O. Petrucci<sup>4, 5</sup>, S. Bianchi<sup>3</sup>, J. S. Kaastra<sup>6, 7, 8</sup>, G. A. Kriss<sup>9, 10</sup>, M. Mehdipour<sup>6, 11</sup>, M. Whewell<sup>11</sup>, N. Arav<sup>12</sup>, E. Behar<sup>13</sup>, R. Boissay<sup>14</sup>, G. Branduardi-Raymont<sup>11</sup>, E. Costantini<sup>8</sup>, J. Ebrero<sup>15</sup>, L. Di Gesu<sup>8</sup>, F. A. Harrison<sup>16</sup>, S. Kaspi<sup>13</sup>, G. Matt<sup>3</sup>, S. Paltani<sup>14</sup>, B. M. Peterson<sup>17, 18</sup>, K. C. Steenbrugge<sup>19</sup>, and D. J. Walton<sup>16, 20</sup>

<sup>1</sup> INAF-IASF Bologna, via Gobetti 101, 40129 Bologna, Italy  
e-mail: massimo.cappi@inaf.it

<sup>2</sup> Max-Planck-Institut für extraterrestrische Physik, Giessenbachstrasse, 85748 Garching, Germany

<sup>3</sup> Dipartimento di Matematica e Fisica, Università degli Studi Roma Tre, via della Vasca Navale 84, 00146 Roma, Italy

<sup>4</sup> Université Grenoble Alpes, IPAG, 38000 Grenoble, France

<sup>5</sup> CNRS, IPAG, 38000 Grenoble, France

<sup>6</sup> SRON Netherlands Institute for Space Research, Sorbonnelaan 2, 3584 CA Utrecht, The Netherlands

<sup>7</sup> Department of Physics and Astronomy, Universiteit Utrecht, PO Box 80000, 3508 TA Utrecht, The Netherlands

<sup>8</sup> Leiden Observatory, Leiden University, PO Box 9513, 2300 RA Leiden, The Netherlands

<sup>9</sup> Space Telescope Science Institute, 3700 San Martin Drive, Baltimore, MD 21218, USA

<sup>10</sup> Department of Physics and Astronomy, The Johns Hopkins University, Baltimore, MD 21218, USA

<sup>11</sup> Mullard Space Science Laboratory, University College London, Holmbury St. Mary, Dorking, Surrey, RH5 6NT, UK

<sup>12</sup> Department of Physics, Virginia Tech, Blacksburg, VA 24061, USA

<sup>13</sup> Department of Physics, Technion-Israel Institute of Technology, 32000 Haifa, Israel

<sup>14</sup> Department of Astronomy, University of Geneva, 16 Chemin d'Ecogia, 1290 Versoix, Switzerland

<sup>15</sup> European Space Astronomy Centre, PO Box 78, 28691 Villanueva de la Cañada, Madrid, Spain

<sup>16</sup> Cahill Center for Astronomy and Astrophysics, California Institute of Technology, Pasadena, CA 91125, USA

<sup>17</sup> Department of Astronomy, The Ohio State University, 140 W 18th Avenue, Columbus, OH 43210, USA

<sup>18</sup> Center for Cosmology & AstroParticle Physics, The Ohio State University, 191 West Woodruff Ave., Columbus, OH 43210, USA

<sup>19</sup> Instituto de Astronomía, Universidad Católica del Norte, Avenida Angamos 0610, 1280 Casilla, Antofagasta, Chile

<sup>20</sup> Jet Propulsion Laboratory, California Institute of Technology, 4800 Oak Grove Drive, Pasadena, CA 91109, USA

Received 9 March 2016 / Accepted 5 April 2016

### ABSTRACT

In 2013, we conducted a large multi-wavelength campaign on the archetypical Seyfert 1 galaxy NGC 5548. Unexpectedly, this usually unobscured source appeared strongly absorbed in the soft X-rays during the entire campaign, and signatures of new and strong outflows were present in the almost simultaneous UV HST/COS data. Here we carry out a comprehensive spectral analysis of all available *XMM-Newton* observations of NGC 5548 (precisely 14 observations from our campaign plus three from the archive, for a total of ~763 ks) in combination with three simultaneous *NuSTAR* observations. We obtain a best-fit underlying continuum model composed by i) a weakly varying flat ( $\Gamma \sim 1.5$ – $1.7$ ) power-law component; ii) a constant, cold reflection (FeK + continuum) component; iii) a soft excess, possibly owing to thermal Comptonization; and iv) a constant, ionized scattered emission-line dominated component. Our main findings are that, during the 2013 campaign, the first three of these components appear to be partially covered by a heavy and variable obscurer that is located along the line of sight (LOS), which is consistent with a multilayer of cold and mildly ionized gas. We characterize in detail the short timescale (mostly ~ks-to-days) spectral variability of this new obscurer, and find it is mostly due to a combination of column density and covering factor variations, on top of intrinsic power-law (flux and slope) variations. In addition, our best-fit spectrum is left with several (but marginal) absorption features at rest-frame energies ~6.7–6.9 keV and ~8 keV, as well as a weak broad emission line feature redwards of the 6.4 keV emission line. These could indicate a more complex underlying model, e.g. a P-Cygni-type emission profile if we allow for a large velocity and wide-angle outflow. These findings are consistent with a picture where the obscurer represents the manifestation along the LOS of a multilayer of gas, which is also in multiphase, and which is likely outflowing at high speed, and simultaneously producing heavy obscuration and scattering in the X-rays, as well as broad absorption features in the UV.

**Key words.** galaxies: active – X-rays: galaxies – galaxies: individual: NGC 5548

## 1. Introduction

Unified models of active galactic nuclei (AGN) have ‘historically’ been proposed as a static unifying view based on a putative dusty molecular torus, where type 1 AGN are seen face-on,

thereby typically unabsorbed and bright, while type 2 sources are seen edge-on, thus typically obscured and faint (Antonucci & Miller 1985). However in recent years, an ever increasing number of type 1 Seyfert galaxies/AGN (up to 20–30% of limited samples) have shown a significant amount of absorption that is

clearly at odds with the source’s optical classifications (Bassani et al. 1999; Cappi et al. 2006; Panessa et al. 2009; Merloni et al. 2014). Such complex, often variable, absorbing structures seem to call for a revision of the static version of unified models into a more complex, maybe dynamical, structure (e.g. Murray et al. 1995; Elvis 2000; Proga 2007).

On the one hand, ionized absorbers (so-called warm absorbers, WA) are nowadays routinely observed as blue-shifted, narrow, and broadened absorption lines in the UV and X-ray spectra of a substantial (certainly greater than 30%) fraction of AGN and quasars (e.g. Blustin et al. 2005; Piconcelli et al. 2005; McKernan et al. 2007; Ganguly & Brotherton 2008). These absorption systems span a wide range of velocities and physical conditions (distance, density, ionization state), and may have their origin in an AGN-driven wind, sweeping up the interstellar medium, or thermally driven from the molecular torus (Blustin et al. 2005) and outflowing at hundreds to few thousands  $\text{km s}^{-1}$  (see Crenshaw et al. 2003a and Costantini 2010 for reviews on the subject). Even more powerful outflows (the so-called ultra fast outflows, UFOs), which are so highly ionized that their only bound transitions left are for Hydrogen- and Helium-like iron, detectable only at X-ray energies, seem to be present in 30–40% of local radio-quiet and radio-loud AGN, with outflow speeds of up to  $\sim 0.3c$  (Pounds et al. 2003a; Tombesi et al. 2010, 2013, 2014; Gofford et al. 2013). Both WA and UFO phenomena have been seen to vary on both short (hours-days) and long (months-years) time-scales (Cappi 2006) for various plausible reasons, such as variations in either the photoionization balance, or the absorption column density and/or covering fraction (Risaliti et al. 2005; Reeves et al. 2014).

On the other hand, there is also mounting evidence for the presence of large columns of additional neutral or mildly ionized gas along the LOS to not only type 2 Seyfert galaxies (e.g. Turner et al. 1997, 1998) but also type 1 and intermediate Seyferts (e.g., Malizia et al. 1997; Pounds et al. 2004; Miller et al. 2007; Bianchi et al. 2009; Turner et al. 2009; Risaliti et al. 2010; Lobban et al. 2011; Marchese et al. 2012; Longinotti et al. 2009, 2013; Reeves et al. 2013; Walton et al. 2014; Miniutti et al. 2014; Rivers et al. 2015). In some cases, the columns are so large that astronomers have called these “changing look” sources (i.e. sources changing from being absorbed by a Compton thin to a Compton thick column density). From the pioneering works of Risaliti et al. (Risaliti et al. 2002, 2005) on a few interesting sources such as the Seyfert 1 NGC 1365, to detailed studies on an increasing number of sources and on systematic studies of larger samples (Markowitz et al. 2014; Torricelli-Ciamponi et al. 2014; Tatum et al. 2013), evidence has accumulated for the importance of large, complex, and variable *neutral* absorption also in type 1 Seyfert galaxies. Current interpretations for this cold circumnuclear gas are clumpy molecular tori (Krolik & Begelman 1988, Markowitz et al. 2014; Hönic 2013), absorption from inner and/or outer BLR clouds (Risaliti et al. 2009), or accretion disc outflows (Elitzur & Shlosman 2006; Proga 2007; Sim et al. 2008).

NGC 5548 ( $z = 0.017$ ) is one of the X-ray brightest ( $2\text{--}10$  keV flux of  $\sim 2\text{--}5 \times 10^{-11}$   $\text{erg cm}^{-2} \text{s}^{-1}$ ), and most luminous ( $L_{2\text{--}10 \text{ keV}} \sim 1\text{--}3 \times 10^{44}$   $\text{erg/s}$ ) Seyfert 1 galaxies known. As such, it is one of the best-studied example of a Seyfert 1 galaxy and has been observed by all major satellites since it entered the Ariel V high galactic latitude source catalog (Cooke et al. 1978). NGC 5548 exhibits all the typical components seen in type 1 Seyfert galaxies, that is: a steep ( $\Gamma \sim 1.8\text{--}1.9$ ) power-law spectrum plus a reflection component with associated FeK line, a soft-excess emerging below a few keV, evidence for warm

ionized gas along the LOS, and typical soft X-ray variability, as shown in the CAIXavar sample by Ponti et al. (2012a). Recently, detailed studies of either the time-average or variability properties of the WA, the reflection component, and the soft-excess component have been made using either low- (CCD-type) or higher- (grating-type) energy resolution instrumentation available from *Chandra*, *XMM-Newton* and *Suzaku* (Pounds et al. 2003a,b; Steenbrugge et al. 2003, 2005; Crenshaw et al. 2003a,b; Andrade-Velazquez et al. 2010; Krongold et al. 2010; Liu et al. 2010; Brenneman et al. 2012; McHardy et al. 2014).

In 2013, our team conducted a long multi-satellite observing campaign on NGC 5548. The campaign is introduced in detail in Mehdipour et al. (2015; hereafter Paper I). The main results from the campaign, the simultaneous appearance of an exceptional obscuring event in the X-rays and a broad absorption line (BAL) structure in the UV, are presented in Kaastra et al. (2014; hereafter Paper O). The shadowing effects of this UV BAL and X-ray obscurer on the larger-scale “historical” UV narrow absorption lines and WA are presented in Arav et al. (2015; hereafter Paper II). The high energy properties of the source during, and before, the campaign are shown in Ursini et al. (2015; hereafter Paper III), while the study of a short-timescale flaring event that happened in September 2013 and which triggered a *Chandra* LETG observation is addressed in Di Gesu et al. (2015; hereafter Paper IV), together with the analysis of the WA short-term variability during this event. The time-averaged soft X-ray line-dominated RGS spectrum is presented and modeled in detail in Whewell et al. (2015; hereafter Paper V). For the longer-term timescales, the historical source behavior is presented in Ebrero et al. (2016a,b; hereafter Paper VI), while the full *Swift* multi-year monitoring is presented in Mehdipour et al. (2016; hereafter Paper VII).

Here, we focus on the detailed model characterization of the obscurer, and of its spectral variability, by making use of all available EPIC (pn+MOS) spectra (during and before the campaign) and simultaneous *NuSTAR* observations (Sect. 2). We also incorporate in our modeling the results from the papers mentioned above, which were obtained during the campaign and which were based on other instruments and satellites, such as RGS spectra, HST/COS spectra, and *Swift* long-term light-curves. This allows us to draw a comprehensive and self-consistent understanding of the obscurer properties (Sect. 4). We then attempt to place constraints on the location and physical origin of the various components required by our model (Sect. 5). Values of  $H_0 = 70 \text{ km s}^{-1} \text{ Mpc}^{-1}$ , and  $\Omega_\Lambda = 0.73$  are assumed throughout, and errors are quoted at the 90% confidence ( $\Delta\chi^2 = 2.71$ ) for 1 parameter of interest, unless otherwise stated.

## 2. Observations and data reduction

NGC 5548 was observed by the *XMM-Newton* EPIC instruments on 17 separate occasions, for a total cleaned exposure time of  $\sim 763$  ks (see Table 1). The first three (archival) observations were performed once in December 2000 and twice in July 2001. The remaining 14 observations were all part of the 2013 multiwavelength campaign (Paper O and Paper I). Twelve observations were performed during the summer 2013, one five months later, in December 2013, and the last one in February 2014. The spacing was intentional to sample different timescales in a rough logarithmic spacing, i.e. multiple on short (days) timescales, and more sparse on longer (months) timescales. A full description of the numerous observations performed during the campaign, from space and ground observatories, is given in Paper I.

**Table 1.** Summary of NGC 5548 *XMM-Newton* (pn) and *NuSTAR* observations.

Obs.	Obs. ID	Start-End date <sup>a</sup>	Exposure <sup>b</sup>	$F_{(0.5-2)}$ <sup>c</sup>	$F_{(2-10)}$ <sup>d</sup>	$F_{(10-30)}$ <sup>e</sup>
<i>Archival data (2000–2001)</i>						
A1	0109960101	2000 Dec. 24–25	16.1	17.2	32.8	–
A2	0089960301	2001 Jul. 09–10	56.7	20.9	40.3	–
A3	0089960401	2001 Jul. 12–12	18.9	28.7	50.8	–
<i>Multiwavelength campaign (2013)</i>						
M1	0720110301	2013 Jun. 22–22	35.4	1.14	15.3	–
M2	0720110401	2013 Jun. 30–30	38.1	3.59	33.0	–
M3	0720110501	2013 Jul. 07–08	38.9	2.16	23.9	–
M4N	0720110601	2013 Jul. 11–12	37.4	3.66	35.8	–
.....	60002044002/3*	2013 Jul. 11–12	51.4	3.66	35.8	51.0
M5	0720110701	2013 Jul. 15–16	37.5	2.62	29.9	–
M6	0720110801	2013 Jul. 19–20	37.1	2.38	30.5	–
M7	0720110901	2013 Jul. 21–22	38.9	2.28	26.3	–
M8N	0720111001	2013 Jul. 23–24	37.5	2.21	27.9	–
.....	60002044005*	2013 Jul. 23–24	49.5	2.21	27.9	45.0
M9	0720111101	2013 Jul. 25–26	32.1	3.14	33.2	–
M10	0720111201	2013 Jul. 27–28	38.9	3.01	32.4	–
M11	0720111301	2013 Jul. 29–30	35.3	2.76	29.6	–
M12	0720111401	2013 Jul. 31–Aug 01	36.1	2.28	26.2	42.8
M13N	0720111501	2013 Dec. 20–21	38.2	2.08	24.9	–
.....	60002044008*	2013 Dec. 20–21	50.1	2.08	24.9	–
M14	0720111601	2014 Feb. 04–05	38.8	3.96	27.2	–

**Notes.** <sup>(a)</sup> Observation start-end dates. <sup>(b)</sup> Net exposure time, after corrections for screening and deadtime, in ks. <sup>(c)</sup> Observed flux in the 0.5–2 keV band, in units of  $10^{-12}$  erg cm<sup>-2</sup> s<sup>-1</sup>. <sup>(d)</sup> Observed flux in the 2–10 keV band, in units of  $10^{-12}$  erg cm<sup>-2</sup> s<sup>-1</sup>. <sup>(e)</sup> Observed flux in the 10–30 keV band, in units of  $10^{-12}$  erg cm<sup>-2</sup> s<sup>-1</sup>. <sup>(\*)</sup> *NuSTAR* observations simultaneous to the *XMM-Newton* observations.

The EPIC data were reduced using the standard software SAS v. 14 (de la Calle 2014) and the analysis was carried out using the HEASoft v. 6.14 package<sup>1</sup>.

After filtering for times of high background rate, and correction for the live time fraction (up to 0.7 for the pn in small window mode), the useful exposure times were typically between 30 and 50 ks per observation (see Table 1). The EPIC pn and MOS cameras were operated in the so-called small window mode with the thin filter applied for all observations, except for the first three archival observations (A1-3) for which the MOS 1 camera was operated in timing mode, thus the MOS1 was not used for this analysis.

Using the `epatplot` command of the SAS, we checked the pattern distributions of the collected events and found that: (i) pile-up was not significant (less than few %) in the pn data at this level of source flux (and notably during the campaign when the source was heavily absorbed), thus we considered both single and double events as per standard procedure and calibrations; (ii) the pattern distribution in the pn deviates significantly below 0.4 keV with respect to model predictions, thus we did not consider the data below 0.4 keV in the present analysis. We note that this is slightly different from our previous analysis reported in Papers 0, III, and IV, in which we always used data down to 0.3 keV. We estimate that the effect of this slightly different choice of low-energy cut-off should nevertheless be largely within statistical errors of the present and previous analysis. Given the significantly lower effective area of the MOS detectors, and for clarity and simplicity, we only report here the results obtained from the pn data and used the MOS data only for consistency checks.

Source counts were extracted from a circular region of 40 arcsec radius, while the background counts were extracted from a nearby source-free and gap-free area of the detector of

the same size. The size of the small window being less than 4.5'×4.5', both source and background were similarly affected by the instrumental Ni and Cu K $\alpha$  lines at 7.3–7.6 keV and 7.8–8.2 keV, respectively, thereby cancelling out their effects.

Finally, we anticipate that all the Fe K line measurements (see Sect. 4.1.2 below) obtained with the pn spectra during the campaign, but not in the earlier archival data, presented a systematic (and more or less constant) blueshift and broadening of the energy scale response by  $\Delta E \sim +30$ –40 eV and  $\sigma(E) \sim 40$ –50 eV, respectively, when compared to the MOS and/or *NuSTAR* independent results. These shifts, albeit being modest, were nevertheless statistically significant and present with either single and double or single-only events, and despite our use of the latest CTI correction files (CCFv45, released in November 2014) and analysis procedure, as described in Smith et al. (2014). To investigate this further, we performed a detailed analysis of the spectral energy scale by comparing our results for different instruments (MOS1, MOS2, pn, and *NuSTAR*), using different pattern selections (from single-only to single+double events), and applying different CTI response correction files (from CCF v27 to v45) which were released in 2013 and 2014. We also compared our results with the energy and width obtained for the AIK line (at 1486 eV) and the MnK doublet (at 5895 and 6489 eV) of the calibration source during a  $\sim 70$  ks CALCLOSED observation performed in 2013, August 31st, i.e. shortly after the campaign and thus representative of the absolute energy scale of the instrument at that time. From this analysis, we attributed both blueshift and broadening to a remaining (admittedly small) uncertainty in the long-term degradation of the EPIC pn CTI, as mentioned in the calibration technical notes of Guainazzi et al. (2014) and Smith et al. (2014). In the following analysis, we thus took into account these systematic shifts and broadenings by using the `zashi ft` and `gsmooth` command in XSPEC to correct for this remaining uncertainty (see also Sect. 4.1.2).

<sup>1</sup> <http://heasarc.gsfc.nasa.gov/docs/software/lheasoft/>

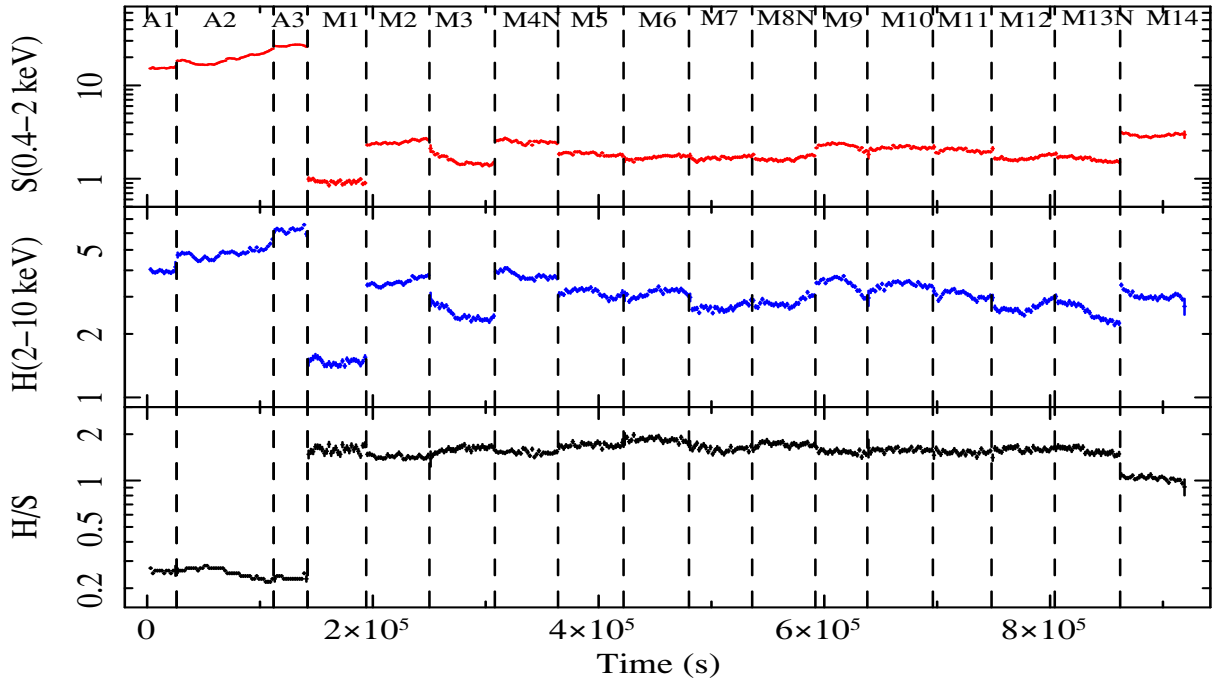


**Fig. 1.** Background subtracted *XMM-Newton* pn light curves of NGC 5548 calculated for the soft (S) 0.4–2 keV energy band (top), the hard (H) 2–10 keV energy band (middle) and their hardness ratios H/S (bottom). Vertical dashed lines indicate when observations were interrupted during the years.

We also used data from three (out of 4) *NuSTAR* observations, those which were simultaneous to the *XMM-Newton* observations, namely the 4th, 8th and 13th observations of the *XMM-Newton* campaign (see Table 1). A comprehensive analysis of the high-energy continuum, combining all available *NuSTAR*, *INTEGRAL*, and previous *BeppoSAX* and *Suzaku* observations is presented in Paper III. We followed their same procedure for the *NuSTAR* data reduction, i.e. we used the standard pipeline (*nupipeline*) of the *NuSTAR* Data Analysis Software (*nustardas*, v1.3.1; part of the *heasoft* distribution as of version 6.14) to reduce the data, and used the calibration files from the *NuSTAR* *caldb* v20130710. The spectra were then extracted from the cleaned event files using the standard tool *nuproducts* for each of the two hard X-ray telescopes aboard *NuSTAR*, which have corresponding focal plane modules A and B (FPMA and FPMB). The spectra from FPMA and FPMB were analyzed jointly, but were not combined. Finally, the spectra were grouped such that each spectral bin contains at least 50 counts.

### 3. Timing analysis

Soft (0.4–2 keV) and hard (2–10 keV) band light curves of NGC 5548 are shown in Fig. 1 (top and middle panels, respectively) with a time bin of 2000 s. Hardness ratios (bottom panel) are also reported to highlight any spectral variations of the source. The light curves include the three archival (year 2000–2001) observations, and the 14 observations of the multifrequency campaign (year 2013–2014), with each observation separated by vertical dotted lines. Within the single observations (including time scales of <few tens of ks) we observe only low/moderate flux variations (less than 20–30 percent of the average flux). However, much stronger flux variations (>50 percent) occur between the different observations, on the time scales sampled by the campaign and longer (i.e. up to years, if we also consider the three archival *XMM-Newton* observations).

As already presented in Papers 0 and I, the hardness ratios show a significant spectral hardening which characterizes the 2013–2014 campaign, when compared to the 2000–2001 archival data. The source does not show any significant spectral variation within each (~half a day long) observation, besides a hint of spectral softening during the last observation. The lack of significant short-term spectral variability justifies our spectral analysis approach below (Sect. 4) of averaging the spectra observation by observation.

To better characterize the distribution of variability power as a function of energy band, we computed the fractional root mean squared (rms) variability amplitude ( $F_{\text{var}}$ ; Nandra et al. 1997; Vaughan et al. 2003; Ponti et al. 2004; Ponti 2007) on both short (hours) and long (days-to-months) timescales. The former is obtained by extracting light curves of the single pn observations, with a time bin of 2 ks, and averaging the  $F_{\text{var}}$  computed from each of them. The latter is obtained by taking the average count rates of each observation and computing the  $F_{\text{var}}$  over the entire campaign, thus sampling timescales going from ~45 ks up to 20 Ms. The light curves are extracted in different energy channels, the width of the channels ensuring the number of counts  $\gg 20$  per time and energy bin. Results are shown in Fig. 2. The  $F_{\text{var}}$  shows, in a clear and model-independent way, that the peak of variability power (~30 percent) lies in the energy band between 1 and 5 keV, and most of the variability occurs on the long timescales. This shape is very similar to what is typically observed also in other Seyfert galaxies (Ponti 2007). Remarkably, a narrow feature is very clearly observed here at the energy of the Fe K $\alpha$  line, which strongly suggests the presence of a constant (on long timescales) reflection component.

It is worth noting that, despite being very low (few percents), the  $F_{\text{var}}$  of the short timescales is significantly different from zero. We verified that this residual variability is most likely to be ascribed to red-noise leakage effects (e.g. Uttley et al. 2002), rather than to intrinsic, short-term variability of the source. In other words, variability over timescales slightly longer than the

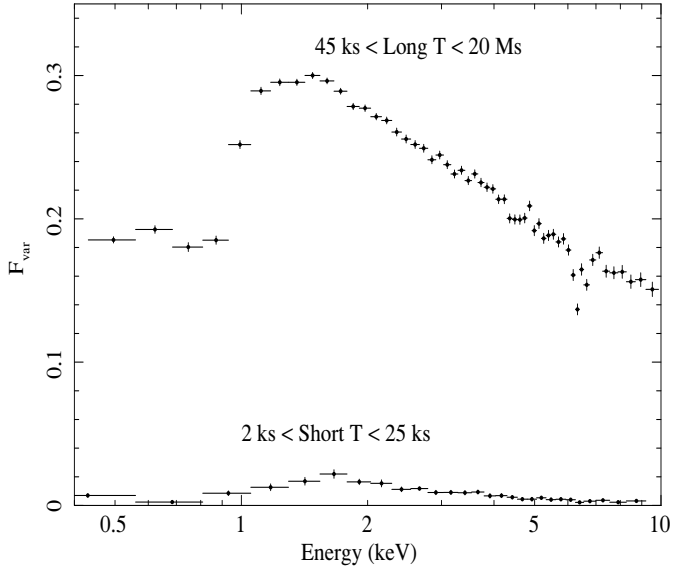


**Fig. 2.** Fractional variability (rms) spectra of NGC 5548 calculated over long (45–2000 ks, top curve) timescales, i.e. longer than observations durations, but shorter than overall campaign, and over short (2–25 ks, bottom curve) timescales, i.e. longer than minimum time bin but shorter than shortest observation duration.

maximum sampled timescale (limited by the duration of the observation) has introduced slow rising and falling trends across the light curve of the single observations, which have contributed to its short-timescale variance. As a consequence, variability power from long timescales has been transferred to the short timescales. Variability studies on even longer timescales than those presented here (using *Swift* light curves) are presented in McHardy et al. (2014) and Paper VII.

#### 4. Spectral analysis

Within each observation, the source varied only very weakly either in flux (top and medium panels of Fig. 1) or in spectral shape (bottom panel of Fig. 1), as found also from the very low  $F_{\text{var}}$  value when calculated on short-timescales (Fig. 2). We thus extracted the mean pn spectra for each of the 17 observations, grouping the data to a maximum of 10 channels per energy resolution element and 30 counts per channel to apply the  $\chi^2$  minimization statistics. In all following fits, the Galactic column density was fixed at the value of  $N_{\text{Hgal}} = 1.55 \times 10^{20} \text{ cm}^{-2}$  (Dickey & Lockman 1990), and abundances were taken from Lodders (2003).

Figure 3 shows the overall *XMM-Newton* spectra during all observations (1–17) which clearly show the strong absorption that is affecting all the 0.3–10 keV spectra during the 2013 campaign (obs. 4–17, in color) when compared to the 2000–2001 archival unabsorbed spectra (obs. 1–3, in black). Figure 4 further illustrates the complex and strongly energy-dependent variability of the source during the campaign: the top two panels show the large and complex variability in the soft 0.4–2 keV (top left panel) and hard 2–7 keV (top right panel). The two bottom panels show the reduction in variability going from lower (7–10 keV) to higher (10–30 keV) energies. Because of the heavy and variable absorption affecting the source, the spectrum is very complex and model parameters (such as the photon index  $\Gamma$ , the absorption column densities, and their covering factors) are often strongly degenerate. Moreover, during the unobserved, archival observations (A1→3) the source shows a very

significant, moderately strong, soft-excess (see e.g. Pounds et al. 2003b) which is however not easy to detect during the monitoring campaign (M1→14) because of the heavy obscuration.

To overcome, or minimize, the above limitations we decided to proceed in the following way: first, we used the three *XMM-Newton* spectra for which *NuSTAR* was simultaneously available, and used data at first only above 4 keV, to obtain the best possible constraints on the underlying source continuum components, in particular the reflection component. Second, we considered also the data below 4 keV, using all information from previous papers in this series and from literature, and also combine the information at soft X-rays obtained from the archival *XMM-Newton* observations. These two different steps and studies (Sects. 4.1 and 4.2) are preliminary and crucial to then best characterize the obscurer variability using the whole dataset of *XMM-Newton* observations.

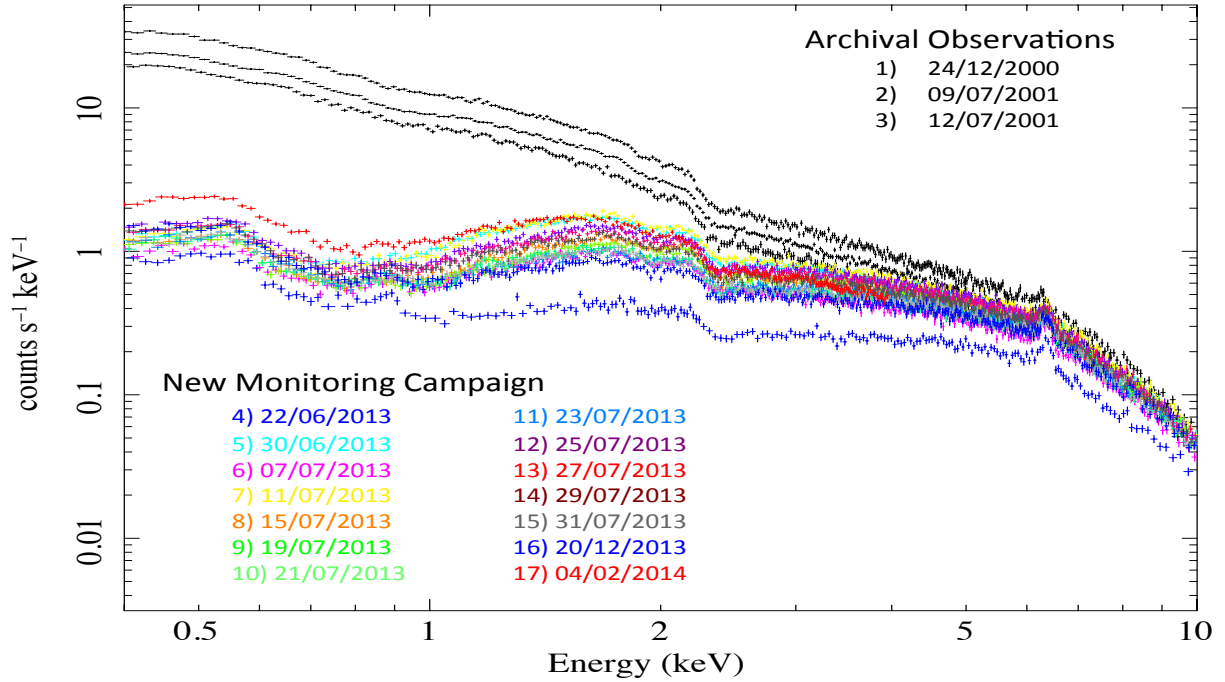
#### 4.1. Hard (>4 keV) X-ray band: underlying continuum and constant reflection component

##### 4.1.1. The three *XMM-Newton*+*NuSTAR* simultaneous observations

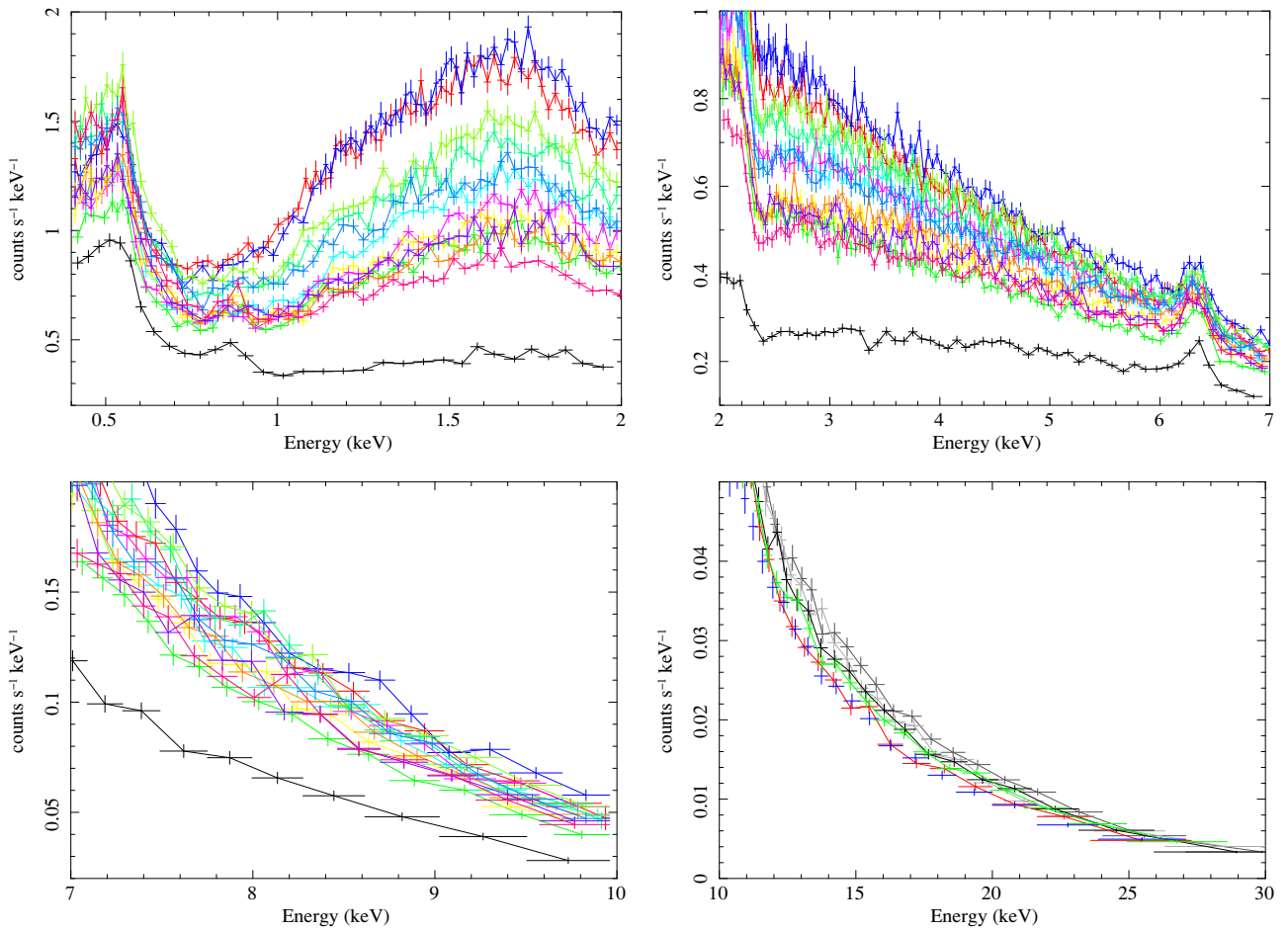
As mentioned above, we first considered only the data in the 4–79 keV interval where the data are less sensitive to the precise modeling of the obscurer, in an attempt to minimize degeneracies induced by the absorbers. *XMM-Newton* and *NuSTAR* spectra were fitted individually for each of the three simultaneous observations, with the same model, but letting all parameters free to vary, except for the normalizations of the two *NuSTAR* modules (FPMA/B), which were kept tied together. For plotting purposes only, and to better identify any systematic deviation from the fits, the spectra were then grouped together (using the `setplot group` command in *XSPEC*) and color-coded with pn spectra in black and *NuSTAR* spectra in red. Cross-normalization values among different instruments (FPMA vs. FPMB vs. pn) were always left free to vary but these were never larger than a few percent, typically 2–3%, in line with expectations (Madsen et al. 2015).

Figure 5 shows the ratios (between ~4–50 keV) obtained from a fit of the 4–79 keV spectra with a single non-absorbed power-law model (with  $\Gamma \sim 1.3$ –1.5). Low energy curvature, a narrow line at ~6.4 keV and a high energy hump between 10–30 keV are readily seen in the data (see Fig. 5, top). We thus added a cold absorption column density plus a Gaussian emission line and a continuum reflection model (`pexrav` in *XSPEC*). Despite the possible presence of additional absorption feature(s) between 7–8 keV (see Fig. 5, bottom panel, and following analysis in Sect. 4.5), the use of a more complex absorber, either partially covering or ionized, was not required here when fitting the continuum above 4 keV, likely because of the strongly curved low-energy cut-off which requires a substantially cold absorber to be modeled, with  $N_{\text{H}} \simeq 4$ –7  $\times 10^{22} \text{ cm}^{-2}$  (Table 2).

Best-fit parameters obtained from *XMM-Newton* only were in very good agreement (typically within a 1- $\sigma$  error) with those obtained with *NuSTAR* only, except for a mildly flatter slope (by  $\Delta\Gamma \sim 0.1$ ) required for *XMM-Newton* with regard to *NuSTAR*. Within each observation, we choose to tie all parameters obtained from both instruments, except for letting their cross-normalizations and photon index free to vary (to take into account the remaining calibration uncertainties), but report here and below values of photon indices and fluxes obtained for the pn only to allow better comparison with observations without the *NuSTAR* simultaneous data. Best-fit values for the three



**Fig. 3.** The 0.4–10 keV spectra of NGC 5548 obtained with the EPIC pn during the three archival observations (black) and during the 14 observations of the 2013 summer campaign (color). Observations are summarized in Table 1.



**Fig. 4.** X-ray spectra obtained during the campaign (M1→M14, including the simultaneous M4N, M8N and M13N *NuSTAR* observations plotted above 10 keV) plotted on linear scales, and with the same factor of  $\sim 10$  extension range (from *bottom to top*) in the *y*-axis scale intensities. These are shown to illustrate the important and complex variability as a function of energy up to 2 keV, and its gradual reduction above 2 keV, and up to 30 keV.

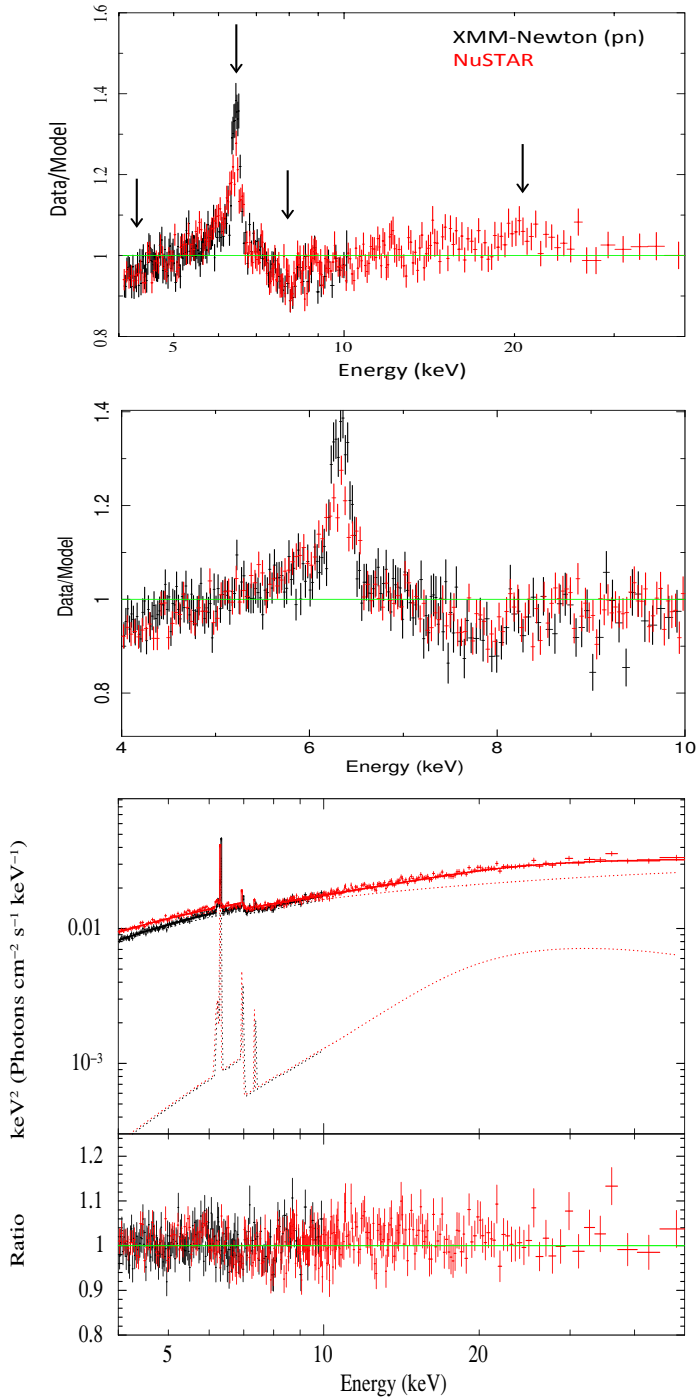


**Fig. 5.** *Top:* data are plotted as the ratio to a single power-law continuum model fitted to the grouped observations M4N, M8N, and M13N with *XMM-Newton* (black) and *NuSTAR* (red) simultaneous data. As indicated by the arrows, going from low to high energies, one can clearly note the presence of: a sharp low-energy cut-off, a narrow Fe K line at  $\sim 6.4$  keV, some absorption feature(s) between 7–8 keV, and a high energy hump between 10–30 keV. *Middle:* same as *top panel*, but zoomed between 4 and 10 keV. *Bottom:* best-fit spectrum, model, and ratios plotted between 4–50 keV (see Sect. 4.1.1 for details).

observations are reported in Table 2. These values are consistent with those obtained by Papers III and IV.

Given the neutral energy for the Fe K line, its narrow width, and its constant intensity, the line is consistent with being produced by reflection from a cold and distant

reflector (see Sect. 5.1 for further discussion). This is consistent with our analysis below (Sect. 4.1.2) using the whole set of *XMM-Newton* observations. This agrees also with our previous (model-independent) findings based on the source fractional variability amplitude (Sect. 3). The line equivalent width ( $EW \sim 70\text{--}110$  eV) with respect to the underlying continuum reflection ( $R \sim 0.56\text{--}0.91$ , see Table 2) is consistent with the line being produced by a plane parallel neutral Compton thick reflector, and solar abundance, thus we decide to choose, for simplicity, the *XSPEC* model *pexmon* (Nandra et al. 2007), which gives a self-consistent description of both the neutral Fe  $K_{\alpha}$  line and the Compton reflection continuum. This model also self-consistently generates the Fe  $K_{\beta}$ , Ni  $K_{\alpha}$ , and Fe  $K_{\alpha}$  Compton shoulder expected from a Compton-thick reflecting medium. Following the results presented in Paper III, we assumed, and fixed, the parameters of the intrinsic continuum illuminating the reflection slab to typical values of  $\Gamma = 1.9$ ,  $E_c = 300$  keV, inclination = 30 deg, and solar abundances. With this model, we obtained the best-fit parameters listed in Table 2. These values are in agreement with those shown in Paper III.

From now on, in this analysis these values will be referred to as our baseline underlying continuum model. Moreover, motivated by the fact that the line intensity did not vary significantly (neither in intensity nor in energy) during the other 14 available observations (see Sect. 4.1.2), we decided to freeze the reflection component to the average value obtained from the three *XMM-Newton* + *NuSTAR* simultaneous observations, i.e. a normalization at 1 keV of  $5.7 \times 10^{-3}$  photons  $\text{keV}^{-1} \text{cm}^{-2} \text{s}^{-1}$ , also in agreement with Paper III.

#### 4.1.2. The whole 17 *XMM-Newton* observations

Given the above results, we thus proceeded in our analysis by adding to the previous observations (M4N, M8N, and M13N) the other 14 available *XMM-Newton* observations, including the three archival observations and the remaining 11 from the 2013 campaign. Again, the spectra were first considered only above 4 keV and focusing on the properties of the Fe K line and reflection component before and during the campaign.

Following the previous analysis, we first fitted all the 17 *XMM-Newton* spectra with a single, cold, absorber plus an Fe  $K_{\alpha}$  line, plus a *pexrav* continuum reflection model. This simple model yielded a good characterization of all *XMM-Newton* spectra, as demonstrated by the grouped spectrum shown in Fig. 6. The time-series for the Fe K line parameters during all 17 observations are shown in Fig. 7. We note that the line energy during the campaign was slightly higher ( $\approx 6.43 \pm 0.01$  keV) than during the first three archival observations ( $\approx 6.39 \pm 0.01$  keV), and was also systematically higher than the energy  $\approx 6.40 \pm 0.01$  keV obtained using only the MOS data. As discussed in Sect. 2, we attribute the energy shift, and slight broadening, of the FeK line to remaining CTI response degradation that has not properly been accounted for.

The line is consistent with being constant in intensity during all the 17 observations (Fig. 7, bottom panel), i.e. not only during the campaign, but also after comparison with the ( $\sim 13$  years) earlier archival observations. Overall, in agreement with our earlier findings, which are based on the fractional variability (Sect. 3), this analysis readily demonstrates that the Fe K line emission is neutral, narrow and, most importantly, constant in time. We thus choose again to model both line and continuum using the self-consistent cold reflection model *pexmon*, and fit all data with the reflection intensity fixed at its average value ( $5.7 \times 10^{-3}$  photons  $\text{keV}^{-1} \text{cm}^{-2} \text{s}^{-1}$ ) obtained in Sect. 4.1.1, and

**Table 2.** Hard (4–79 keV) X-ray continuum emission (*XMM-Newton* + *NuSTAR* observations): Power law plus reflection models.

<i>Phenomenological reflection model (cut-off-PL + Fe <math>K_{\alpha}</math> emission line + pexrav)</i>										
Obs. N.	Obs. name	$N_{\text{H}}$ ( $\times 10^{22}$ cm $^{-2}$ )	$\Gamma$	$E_c$ (keV)	Energy <sup>1</sup> (keV)	$EW^2$ (eV)	Int. <sup>3</sup> ( $\times 10^{-5}$ )	$R$ ( $\Omega/2\pi$ )	$A_{\text{norm}}$ ( $\times 10^{-3}$ )	$\chi^2/\nu$
7	M4N	$4.1 \pm 0.5$	$1.74 \pm 0.04$	$>313$	$6.35 \pm 0.02$	$69 \pm 9$	3.0	0.56	$5.9^{+0.9}_{-1.3}$	3535/3471
11	M8N	$7.2^{+0.5}_{-1.0}$	$1.75 \pm 0.06$	$>212$	$6.38 \pm 0.02$	$83 \pm 10$	3.0	0.65	$6.2^{+1.1}_{-1.4}$	3535/3471
16	M13N	$5.8^{+0.6}_{-1.2}$	$1.60 \pm 0.04$	$129^{+48}_{-30}$	$6.42 \pm 0.02$	$110 \pm 10$	3.7	0.91	$5.9^{+1.0}_{-0.5}$	3535/3471
<i>Physical and self-consistent reflection model (cut-off-PL + pexmon)</i>										
Obs. N.	Obs. name	$N_{\text{H}}$ ( $\times 10^{22}$ cm $^{-2}$ )	$\Gamma$	$E_c$ (keV)	$R$ ( $\Omega/2\pi$ )	$A_{\text{norm}}$ ( $\times 10^{-3}$ )	$\chi^2/\nu$			
7	M4N	$3.8 \pm 0.7$	$1.73 \pm 0.02$	$>310$	0.51	$5.4 \pm 0.5$	1234/1157			
11	M8N	$5.5 \pm 0.8$	$1.63 \pm 0.05$	$157^{+153}_{-54}$	0.79	$6.0 \pm 0.5$	1178/1157			
16	M13N	$5.7 \pm 1.2$	$1.60 \pm 0.06$	$123^{+109}_{-41}$	0.95	$6.2 \pm 0.5$	1153/1157			

**Notes.** <sup>(1)</sup> Emission line rest-frame energy centroid, in units of keV. <sup>(2)</sup> Emission line rest-frame equivalent width in units of eV. The width of the line was fixed to  $\sigma = 0.1$  keV (see text for details). <sup>(3)</sup> 2–10 keV flux in units of  $10^{-11}$  erg s $^{-1}$  cm $^{-2}$ .

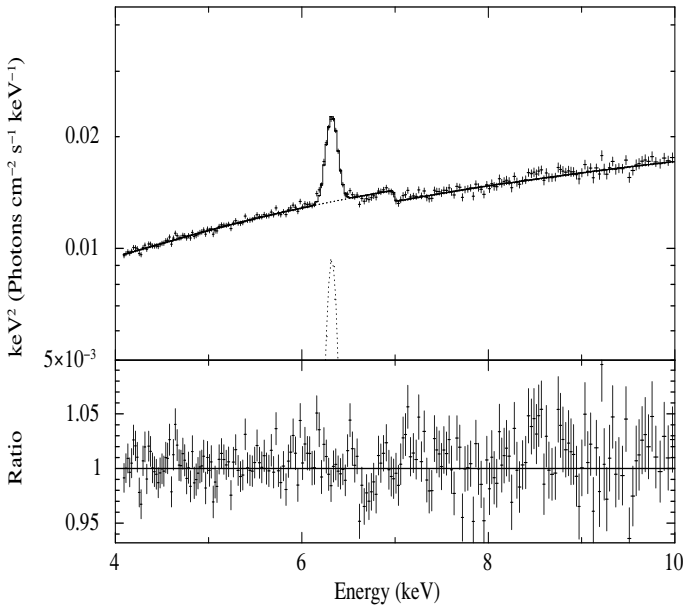


**Fig. 6.** The 4–10 keV band spectrum obtained from the individual fitting of all the 17 *XMM-Newton* spectra, and the data/model ratios, grouped in a single dataset.

then freezing the *zshift* parameter to its best-fit value. We note that this simple analysis readily shows that, during the campaign, the photon index was flatter ( $\Gamma \sim 1.5$ – $1.7$ ) than typically found during either the three archival observations or historically in this source ( $\Gamma \sim 1.7$ – $1.9$ , e.g. Dadina 2007), and despite allowing in the fit for large absorption column densities with values between  $\log N_{\text{H}} \sim 22$ – $23$  cm $^{-2}$ .

#### 4.2. Soft (<4 keV) X-ray band: warm absorber, intrinsic soft-excess and scattered component

As mentioned above, the soft ( $E < 4$  keV) X-ray spectrum of this source is known to be rather complex. Historically, it is known to require at least two components to be properly modeled, such as a complex, multi-temperature warm absorber, plus an intrinsic soft X-ray emission component (commonly called soft-excess). In this part of the spectrum, we require at least one additional component, a soft scattered component, to be consistent with

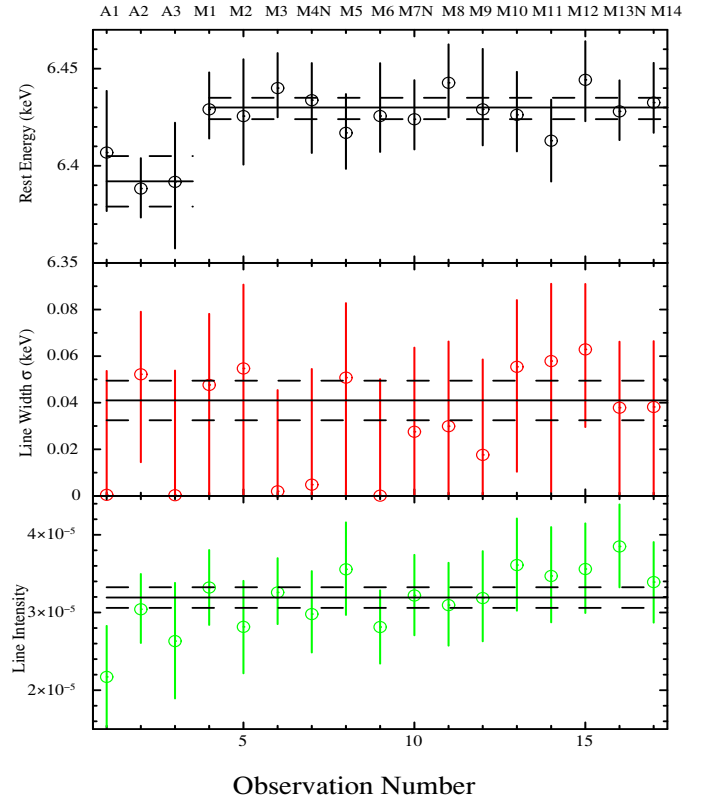


**Fig. 7.** Time series of the FeK line best-fit parameters: Rest-frame energy (*top*, black) in keV, line width (*middle*, red) in keV, and line intensity (*bottom*, green) in photons cm $^{-2}$  s $^{-1}$  in the line. Best-fit values and 1-sigma (68%) errors for a fit with a constant value are shown.

earlier and present observations. Below, we briefly address the evidence and need for each of these three components, even before considering the complex (and variable) obscurer found during the campaign, and which will be discussed only afterwards.

*Warm absorber:* following the analysis of Paper 0, we have added into our model a constant column density warm absorber model calculated from the same SED as discussed in Papers I and II. This component absorbs only the baseline underlying continuum model, and not the soft emission lines introduced below (which are already corrected for absorption from the WA, as discussed below), and it accounts for the historical multi

components highly ionized warm absorber that is clearly seen when the source is in its typical unobscured state (Kaastra et al. 2002, 2004; Steenbrugge et al. 2003, 2005; Krongold et al. 2010; Andrade-Velazquez et al. 2010; Paper VI). Absorption from this warm absorber component was clearly detected during the unobscured archival observations and, given the pn low energy resolution, its six WA ionization components could be approximated by only two warm absorber ionization components with ionization parameters<sup>2</sup>  $\log \xi \approx 1-2.7 \text{ erg cm s}^{-1}$  and low column density ( $\log N_{\text{H}} \approx 21-22 \text{ cm}^{-2}$ ), which is consistent with previous literature results (Krongold et al. 2010). The effect of this multi-component WA is less visible, but still significant, on the spectra during the campaign when the source is highly obscured (see the transmission curve of this component in Fig. S3 of Paper 0). Following Paper 0 and II, we also know from the UV spectra that the kinematics of the warm absorber have not changed over the last 16 years, and Paper VI shows that all historical data on NGC 5548 are consistent with a multi-component WA which is assumed to vary in response to changes in the underlying flux level only. For the obscured states, we thus kept the warm absorber parameters frozen at their average value found by Paper 0, and calculated using an ionization balance, which assumes illumination from the average obscured SED.

*Soft-excess intrinsic emission:* NGC 5548 is known to have a clear and strong soft-excess intrinsic continuum (see e.g. Kaastra & Barr 1989; Kaastra et al. 2000, 2002; Steenbrugge et al. 2003, 2005). Even if there is no direct evidence for the presence of this same soft-excess during the campaign, because of the strong obscuration, it is important to model it to our best to reduce as much as possible the parameter degeneracies in our following analysis of the multilayer obscurer variability (see Sect. 4.3.2). We thus performed a re-analysis of the 3 *XMM-Newton* archival observations (A1→A3), when the source was in its typical unobscured state. We first used the same baseline model (Power law plus reflection component) as for the high energy part of the spectrum (Sect. 4.1.1) and the above warm absorber affecting only the lower energies. We confirm the results obtained by Pounds et al. (2003b) who analyzed the *XMM-Newton* spectra of A2+A3 to simultaneous data from the MECS+PDS onboard *BeppoSAX*: a weak soft excess is seen, after allowing for the overlying absorption, as a smooth upward curvature in the X-ray continuum below  $\sim 2 \text{ keV}$ . Unlike Pounds et al. (2003b), we do not attempt here to test different models<sup>3</sup> for the soft-excess component, nor try to constrain in detail its shape nor intensity during A1→A3. This would be beyond the scope of this paper. Instead, we choose a Comptonization model, which is able to describe the soft X-ray continuum in a way that is consistent with the source UV-to-soft X-ray properties seen before, during, and after the campaign, as shown in Paper VII. In fact, the long-term and broad-band UV-to-soft X-ray analyses presented in Papers I and VII, using *Swift* data, indicate a correlation between the far UV and soft-X-ray emission, which suggests the presence of an intrinsic emission component linking the UV to the soft-X-rays, similar to the one measured in Mrk 509 (Mehdipour et al. 2011; Petrucci et al. 2013), and is possibly due to thermal Comptonization. We thus include in our fits the same thermal Comptonization model

(*Comptt*) as in Paper I, fixing the shape at the best-fit values found in Paper VII, but allowing its normalization to be a free parameter in our fits. A similar approach was taken in Paper IV, but fixing the normalization to the value expected by adopting the correlation measured by Paper I and VII.

*Scattered component:* in all our models we include a soft scattered component to account for the narrow emission lines that are clearly detected in the higher resolution data available from the RGS instruments between 0.3–2 keV in the obscured states. We make use of the results obtained from the detailed analysis of Paper V. Their analysis shows that the RGS spectrum is clearly dominated by narrow emission lines (see their Fig. 1), and that these are consistent with being constant in flux during the whole campaign. We therefore prefer to use here, and include in our model, the average best-fit model obtained in Paper V using the whole 770 ks RGS stacked spectrum, rather than use the lower statistics observation by observation and, as a consequence, have to deal with cross-instrument calibration issues (but see Paper IV for addressing some of these issues). This average emission line model was calculated using the spectral synthesis code *Cloudy* (version 13.03; Ferland et al. 2013), the unabsorbed SED calculated in Paper I, and was used as a fixed table model in the fit in *XSPEC*. This reproduces well, and self-consistently, all the narrow emission lines, including the He-like triplets of Neon, Oxygen, and Nitrogen, the radiative recombination continuum (RRC) features, and the (Thomson electron) scattered continuum seen in the RGS spectrum (see Fig. 6 in Paper V). The best-fit parameters of the emitting gas are  $\log \xi = 1.45 \pm 0.05 \text{ erg cm s}^{-1}$ ,  $\log N_{\text{H}} = 22.9 \pm 0.4 \text{ cm}^{-2}$  and  $\log v_{\text{turb}} = 2.25 \pm 0.5 \text{ km s}^{-1}$ . The emission model also requires, and includes, absorption from at least one of the six components of the warm absorber found by previous analyses of these and historical data (see Paper V for more details). For the purposes of the present broadband modeling, this same *Cloudy* model was extended up to  $E \sim 80 \text{ keV}$ , which corresponds to the high-energy limit of the *NuSTAR* spectral band, by accounting for Compton and resonant scattering up to these higher energies and including the expected weak FeK emission lines produced by this Compton thin layer of gas. The contribution from this component to the broad-band model is shown in the unfolded spectrum of Fig. 8 (dashed red line in panel e). Its contribution to the soft (0.5–2 keV) X-ray flux is  $\sim 1.8 \times 10^{-13} \text{ erg cm}^{-2} \text{ s}^{-1}$ , and corresponds to about 8% of the total soft X-ray flux while, in the hard (2–10 keV) band, it is  $\sim 4.8 \times 10^{-13} \text{ erg cm}^{-2} \text{ s}^{-1}$  (i.e.  $\sim 2\%$  of the total flux, and a factor of  $\sim 3$  lower than the reflection component). As discussed in Paper V, this component is consistent with being produced by (photo-ionized) scattered emission from a distant narrow line region (NLR) at a distance of  $\sim 14 \text{ pc}$  from the central source.

#### 4.3. Total (0.4–78 keV) X-ray band: the multilayer obscurer(s)

##### 4.3.1. The three *XMM-Newton*+*NuSTAR* simultaneous observations

We proceeded by now fitting the whole data down to 0.4 keV starting again with the three *XMM-Newton*+*NuSTAR* simultaneous observations only to obtain a best-fit model over the full energy band available. As for the previous analysis, we fit the three observations independently, but using the same model and grouping the *XMM-Newton* spectra together, and then the *NuSTAR* spectra together. The grouping is intended to maximize the statistical deviations (and residuals) from the adopted

<sup>2</sup> The ionization parameter  $\xi$  is defined here as  $\xi \equiv \frac{L}{n_{\text{H}} r^2}$ , where  $L$  is the luminosity of the ionising source over the 13.6 eV-infinity band in  $\text{erg s}^{-1}$ ,  $n_{\text{H}}$  the hydrogen density in  $\text{cm}^{-3}$ , and  $r$  the distance between the ionised gas and the ionising source in cm.

<sup>3</sup> The soft-excess could be modeled by Pounds et al. (2003b) either by two black-body models, a single-temperature Comptonized thermal emission, or enhanced highly ionized reflection from an accretion disc.

**Table 3.** *XMM-Newton* + *NuSTAR* observations: 0.4–79 keV best-fit model (cut-off-PL + soft-excess Comptt emission + *pexmon* + scattered component + two partially covering ionized obscurers).

Obs. N.	Obs. name	$\Gamma$	$\log N_{\text{H},1}$ ( $\text{cm}^{-2}$ )	$C_{f,1}$	$\log \xi_1$ ( $\text{erg cm s}^{-1}$ )	$\log N_{\text{H},2}$ ( $\text{cm}^{-2}$ )	$C_{f,2}$	$\log \xi_2$ ( $\text{erg cm s}^{-1}$ )	$A_{\text{comptt}}$	$\chi^2_{\text{red}}(\chi^2/\nu)$
7	M4N	$1.56 \pm 0.01$	$22.13 \pm 0.01$	$0.87 \pm 0.01$	$< -0.2$	$> 23.1$	$0.21^{+0.02}_{-0.06}$	$\equiv -1$	$30.8^{+21.6}_{-2.9}$	1.15(1555/1348)
11	M8N	$1.60 \pm 0.05$	$22.37 \pm 0.03$	$0.87 \pm 0.02$	$0.75^{+0.08}_{-0.41}$	$23.2 \pm 0.09$	$0.44 \pm 0.05$	$\equiv -1$	$21.4^{+14.3}_{-12.3}$	1.03(1392/1348)
16	M13N	$1.54 \pm 0.06$	$22.35 \pm 0.04$	$0.87 \pm 0.01$	$0.50^{+0.18}_{-0.81}$	$23.2 \pm 0.09$	$0.46 \pm 0.05$	$\equiv -1$	$64.2^{+26.5}_{-14.3}$	1.02(1371/1348)

model, thereby helping to identify any missing model component/feature that would be present in all three spectra, but not included in the model. Following the results discussed above, we incorporate in our broadband model the following emission components:

- i) a power-law continuum;
- ii) a cold and constant reflection component (Sect. 4.1.1);
- iii) a (soft) thermal Comptonization emission model (Sect. 4.2);
- iv) a scattered emission-line dominated component (Sect. 4.2);
- v) the de-ionized WA, as given in Paper 0 (Sect. 4.2), and;
- vi) up to two new absorbing column densities (called “obscurer” components hereinafter, following the name given by Paper 0 to distinguish them from the WA component) to account for the heavy and complex obscuration seen in the spectra.

We note that the obscurer only covers the power-law continuum plus the thermal Comptonization emission, while it does not cover either the reflection continuum or the scattered components. We started with one single neutral and fully covering obscurer, then left its ionization parameter free to vary, then its covering factor, and then both parameters. We then added a second obscurer along the LOS, and repeated the procedure until a best-fit was found, checking that every additional model parameter was statistically required (using the F-test statistical test). Some of the data-to-model residuals obtained during this procedure are shown in Fig. 8 (panels a–e).

Large residuals are obtained when fitting the obscurer with a single, fully covering, either neutral absorber (panel a) or an ionized one (panel b). We made numerous attempts to fit the obscurer with a single, fully covering, ionized absorber using either a “standard” SED for the source (typical of when the source was in its unabsorbed state) or an “obscured” SED (typical of the source absorbed state during the campaign) as input for our *Cloudy* table model. No matter which SED was chosen nor the wide range of parameters used in these fits ( $\log \xi \sim 0.1$ – $4 \text{ erg cm s}^{-1}$ ,  $\log N_{\text{H}} \sim 20$ – $24 \text{ cm}^{-2}$ ), a single fully covering ionized obscurer is clearly inadequate (panel b of Fig. 8) in producing simultaneously the smooth curvature below 4 keV, followed by the upward emission below 1 keV. Actually, very little difference between the two SEDs were recorded in fitting the pn data, in either the best-fit parameters or residuals obtained. Much better fits and residuals were instead obtained when allowing for the obscurer to partially cover the source (panel c), yielding covering factors of  $C_{f,1} \sim 0.84$ – $0.94$ .

We then proceeded to add a second, independent, absorbing column density covering the same underlying continuum, and again contributing to explain the so-called flat low-energy curvature between 1–4 keV. The fit improvement was substantial ( $\Delta\chi^2 \sim 200$ ) and we reached satisfactory fits ( $\chi^2_{\nu} \sim 1$ – $1.2$ ) with a double obscurer partially covering the source, with  $C_{f,2} \sim 0.2$ – $0.4$ , and for which we allowed the ionization parameter of the lowest column density to be free to vary (Fig. 8, panel d). Best-fit values are given in Table 3 and indicate that, based on this

first analysis of the 3 *XMM-Newton*+*NuSTAR* observations, the obscurer is better described by at least two different column densities, one of which is mildly ionized and the other one essentially cold, both of which partially cover the source (Fig. 8, panels d and e). Using the same best-fit model, we then attempt to fit each of the remaining *XMM-Newton* observations individually to understand which of the obscurer parameter(s) is driving the complex variability (Sect. 4.3.2).

We note that, despite our efforts to use physically well motivated and sophisticated models (such as *Cloudy*), and apply these to all sets of observational data available during the campaign (from the UV to the hard X-rays, i.e. Papers I to VII of this series) in a consistent picture, we are left with residuals of emission/absorption line-like features below 1 keV, around 2 keV, and around 6 keV. Albeit rather weak (typically a few eV equivalent width), they are statistically significant, owing to the very high statistics ( $>1$  million counts in total) achieved when grouping the three *XMM-Newton*+*NuSTAR* spectra. We address these one by one. The residuals around 2 keV are probably ascribed to remaining systematic calibration uncertainties owing to the detector quantum efficiency at the Si K-edge (1.84 keV) and mirror effective area at the Au M-edge ( $\sim 2.3$  keV). This was also found in Papers 0, III, and IV, and it was then decided to cut this part of the spectrum out, also to avoid inconsistencies with the RGS spectra, which suffered less from such calibration effects. Features at energies lower than  $\sim 1.5$  keV could be modeled by a combination of a few narrow absorption and/or emission lines at energies around  $\sim 0.5$ – $0.6$  keV and  $1$ – $1.1$  keV, and EW variable between  $\sim 8$ – $15$  eV, depending on the line and observation considered. We estimate that the origin of these features could be ascribed to either remaining uncertainties in the CTI-energy scale at low energies in the pn data, which we know were important during these observations, or to an improper (or approximate) modeling of the emission and absorption lines. In the latter case, uncertainties may be ascribed to the use of the average best-fit models for the warm absorber and the scattered component (see Fig. 6 of Paper V), as well as a too approximate calculation for the Fe UTA atomic structures (at  $\sim 0.7$ – $0.8$  keV, Behar et al. 2001) in the *Cloudy* models. Also a different intrinsic broadening and/or blueshift of either the warm absorber, the scattered component and/or the obscurer itself, which the current pn data does not allow to properly constrain, may also play a role here. Lastly, the possible origin of the remaining features at around 6–7 keV will be addressed below (Sect. 4.5) after investigation of also all the remaining *XMM-Newton* observations.

#### 4.3.2. The whole 17 *XMM-Newton* observations: variability of the multi-layer obscurer

We then applied the best-fit model obtained for the 3 *XMM-Newton* + *NuSTAR* simultaneous observations to the whole set of 17 observations (Sect. 4.3.1), i.e. including a constant soft scattered component, a constant warm absorber, a constant reflection component, plus two absorbing column densities,

**Table 4.** Whole *XMM-Newton* and *XMM-Newton+NuSTAR* observations: 0.4–10 keV best-fit model (cut-off-PL + soft-excess *Comptt* emission + *peXmon* + scattered component + two partially covering ionized obscurers).

Obs. N.	Obs. name	$\Gamma$	$\log N_{\text{H},1}$ ( $\text{cm}^{-2}$ )	$C_{f_1}$	$\log \xi_1$ ( $\text{erg cm s}^{-1}$ )	$\log N_{\text{H},2}$ ( $\text{cm}^{-2}$ )	$C_{f_2}$	$\log \xi_2$ ( $\text{erg cm s}^{-1}$ )	$A_{\text{comptt}}$	$\chi^2_{\text{red}} (\chi^2/\nu)$
1	A1	$1.76 \pm 0.02$	$21.38 \pm 0.04$	$\equiv 1$	$1.07 \pm 0.16$	$21.82 \pm 0.17$	$\equiv 1$	$2.69^{+0.07}_{-0.15}$	$72.2 \pm 5.8$	1.25(528/423)
2	A2	$1.79 \pm 0.02$	$21.32 \pm 0.03$	$\equiv 1$	$1.05 \pm 0.09$	$22.02 \pm 0.07$	$\equiv 1$	$2.72 \pm 0.04$	$58.3 \pm 4.0$	2.14(904/423)
3	A3	$1.82 \pm 0.02$	$21.33 \pm 0.04$	$\equiv 1$	$1.10 \pm 0.11$	$21.82^{+0.13}_{-0.20}$	$\equiv 1$	$2.70^{+0.05}_{-0.19}$	$92.5 \pm 7.5$	1.40(593/423)
4	M1	$1.57 \pm 0.07$	$22.71 \pm 0.06$	$0.84 \pm 0.02$	$< 0.66$	$> 23.1$	$0.44^{+0.08}_{-0.16}$	$\equiv -1$	$< 6.6$	1.23(520/423)
5	M2	$1.61 \pm 0.07$	$22.17 \pm 0.03$	$0.87 \pm 0.03$	$0.57^{+0.03}_{-0.16}$	$> 23.1$	$0.19 \pm 0.02$	$\equiv -1$	$7.8^{+2.3}_{-2.3}$	1.41(596/423)
6	M3	$1.44 \pm 0.08$	$22.28 \pm 0.07$	$0.78 \pm 0.04$	$< 2.5$	$> 23.4$	$< 0.24$	$\equiv -1$	$< 11.5$	1.12(473/423)
7	M4N	$1.56 \pm 0.07$	$22.13 \pm 0.01$	$0.87 \pm 0.01$	$< -0.2$	$> 23.1$	$0.21^{+0.02}_{-0.06}$	$\equiv -1$	$30.8^{+21.6}_{-2.9}$	1.15(1555/1348)
8	M5	$1.67 \pm 0.07$	$22.30 \pm 0.03$	$0.94 \pm 0.02$	$0.61^{+0.14}_{-0.18}$	$23.33 \pm 0.11$	$0.31 \pm 0.09$	$\equiv -1$	$69.8^{+25.3}_{-33.8}$	1.14(482/423)
9	M6	$1.55 \pm 0.07$	$22.35 \pm 0.05$	$0.88 \pm 0.03$	$0.02^{+0.55}_{-0.02}$	$23.11^{+0.18}_{-0.42}$	$0.22 \pm 0.09$	$\equiv -1$	$23.3^{+21.6}_{-12.6}$	1.25(530/423)
10	M7	$1.55 \pm 0.08$	$22.27 \pm 0.05$	$0.89 \pm 0.03$	$0.67^{+0.10}_{-0.26}$	$23.30 \pm 0.13$	$0.37 \pm 0.10$	$\equiv -1$	$26.01^{+19.7}_{-13.5}$	1.16(492/423)
11	M8N	$1.60 \pm 0.05$	$22.37 \pm 0.03$	$0.87 \pm 0.02$	$0.75^{+0.08}_{-0.41}$	$23.2 \pm 0.09$	$0.44 \pm 0.05$	$\equiv -1$	$21.4^{+14.3}_{-12.3}$	1.03(1392/1348)
12	M9	$1.70 \pm 0.07$	$22.29 \pm 0.03$	$0.93 \pm 0.02$	$0.77^{+0.06}_{-0.12}$	$23.31^{+0.09}_{-0.12}$	$0.33 \pm 0.08$	$\equiv -1$	$84.1^{+68.3}_{-42.3}$	1.08(458/423)
13	M10	$1.67 \pm 0.07$	$22.28 \pm 0.02$	$0.94 \pm 0.02$	$0.62 \pm 0.11$	$23.36 \pm 0.09$	$0.32 \pm 0.08$	$\equiv -1$	$127.0 \pm 48$	1.17(503/423)
14	M11	$1.57 \pm 0.08$	$22.23 \pm 0.04$	$0.91 \pm 0.03$	$0.57^{+0.15}_{-0.24}$	$23.26^{+0.11}_{-0.17}$	$0.30 \pm 0.09$	$\equiv -1$	$74.8^{+47.2}_{-26.8}$	1.15(488/423)
15	M12	$1.54 \pm 0.08$	$22.29 \pm 0.05$	$0.87 \pm 0.04$	$0.54^{+0.23}_{-0.54}$	$23.28^{+0.12}_{-0.16}$	$0.35 \pm 0.07$	$\equiv -1$	$30.5^{+19.6}_{-13.4}$	1.12(475/423)
16	M13N	$1.54 \pm 0.07$	$22.35 \pm 0.04$	$0.87 \pm 0.01$	$0.50^{+0.18}_{-0.81}$	$23.2 \pm 0.09$	$0.46 \pm 0.05$	$\equiv -1$	$64.2^{+26.5}_{-14.3}$	1.02(1371/1348)
17	M14	$1.61 \pm 0.06$	$22.01 \pm 0.05$	$0.89 \pm 0.02$	$0.85 \pm 0.03$	$> 23.39$	$0.17 \pm 0.07$	$\equiv -1$	$67.7 \pm 13.2$	1.43(605/423)

which partially obscure the primary power-law continuum, plus the *Comptt* soft-excess component. Each observation was fitted independently letting the parameters of the two ionized absorber(s), the power law (its photon index and normalization), and the normalization of *Comptt* free to vary.

Best-fit values obtained for all 17 observations are shown in Table 4, and indicate that each observation was well described by the above best-fit model, where the obscurer is a combination of one mildly ionized ( $\log \xi_1 \sim 0.5\text{--}0.8$ ), which almost totally covers ( $C_{f_1} \sim 0.8\text{--}0.9$ ) the source with a column density of  $\log N_{\text{H},1} \sim 22.2\text{--}22.7 \text{ cm}^{-2}$ , plus one cold/neutral ( $\log \xi_2$  always less than 0.2, thus fixed at -1) absorber with a larger column of  $\log N_{\text{H},2} \sim 23.2\text{--}23.4 \text{ cm}^{-2}$ , partially covering ( $C_{f_2} \sim 0.2\text{--}0.4$ ) the source. We note that during the first three archival observations, when the source was unobscured, the best-fit parameters of our *Cloudy* models converged into a two-component warm absorber solution that is consistent with the values reported by the *Suzaku* data (Krongold et al. 2010), and which were considered a good approximation, at low energy resolution, of the multi-temperature warm absorber detected in grating *Chandra* and *XMM-Newton* spectra (Andrade-Velazquez et al. 2010; Steenbrugge et al. 2005; Paper VI). During the campaign, our best-fit values are overall in agreement with the average values found by Paper 0 and the independent measurements from Di Gesu et al. (2015), except for the much larger value of  $\xi_1$  found here with respect to Paper 0 and Paper IV, who found a  $\log \xi_1 = -1.2 \pm 0.08$ . There are multiple possible reasons for this apparent discrepancy. First, our analysis is performed observation-by-observation and accounts for the strong soft X-ray spectral variability, while our earlier analysis in Paper 0 reported the time-average values, and Paper IV fixed their ionization parameters to the average values obtained in Paper 0. Second, we used *Cloudy* and the latest results from Paper V to model the ionized absorbers/emitters, while previous analysis in Paper 0 and Paper IV used the *xabs* model in *SPEX*. This may have introduced some systematic differences, in particular in modeling the RRC and Fe-UTA (see also Paper V). Finally, as mentioned above (Sect. 4.3.1), weak but statistically significant residuals are left below  $\sim 1 \text{ keV}$ , and between  $1.8\text{--}2.5 \text{ keV}$ , which may be attributed to remaining calibration uncertainties of the pn spectra. In Papers 0 and III, the first were fitted by adding a few

emission and absorption lines in the average spectra, while the latter energy band was excluded in their analysis. We tested on the three *XMM-Newton+NuSTAR* spectra that adding a few ad-hoc emission and/or absorption lines would indeed contribute to decrease the ionization parameter  $\xi_1$  down to values ( $\sim 0.3$ ) where it becomes rather unconstrained and degenerate with the other parameters, though maintaining an overall best-fit that is substantially unchanged. We thus attribute to at least one of the above reasons the apparent discrepancy in  $\xi_1$ , which should not however have any implication on the analysis below and which focuses on the variability, i.e. the relative intensity, of the most intense features measured observation by observation. But we stress that the absolute value of this parameter must be considered model- and calibration-dependent, thus poorly constrained, by the present analysis.

To further compare with Papers I, IV, and VII, we also tried to either (i) fix the intensity of the Comptonization component to those values predicted from the measured UV flux, and following the UV-soft-X correlation found as given in Paper VII or (ii) to link any of the free parameters ( $\Gamma$ ,  $N_{\text{H},1}$ ,  $C_{f_1}$ ,  $N_{\text{H},2}$ ,  $C_{f_2}$ ,  $A_{\text{comptt}}$ ) listed in Table 4 to a same constant value. The fits always returned significantly worse statistical values (by at least  $\Delta\chi^2 > 10$ ) in at least a few observations, supporting the need for all those free parameters. The drawback here being that, in some observations, the model is clearly over-fitting the data and yields poorly constrained parameters (e.g. during M3).

We then investigated the time evolution of all those parameters left free to vary, searching also for trends and correlations among them. In the top of Fig. 9, we plot the 7–10 keV flux light curve, since the flux in this energy band should have very little, if any, sensitivity to the obscuration. Interestingly, the source fluxes between 7–10 keV during the archival observations (first three observations), the average historical values (Paper VI), and during the campaign (last 14 observations) are all comparable within a factor of  $\sim 2$ . Moreover, except for observation M3, which shows the flattest of all photon index measurements ( $\Gamma \sim 1.44$ ), all other values of the photon index are within the lower and higher limits (i.e.  $1.54\text{--}1.79$ , see Table 3) found from the 3 *XMM-Newton + NuSTAR* broadband fits, i.e. should really be indicative of the intrinsic power-law continuum underlying shape. This readily suggests that most of the flux and spectral variability

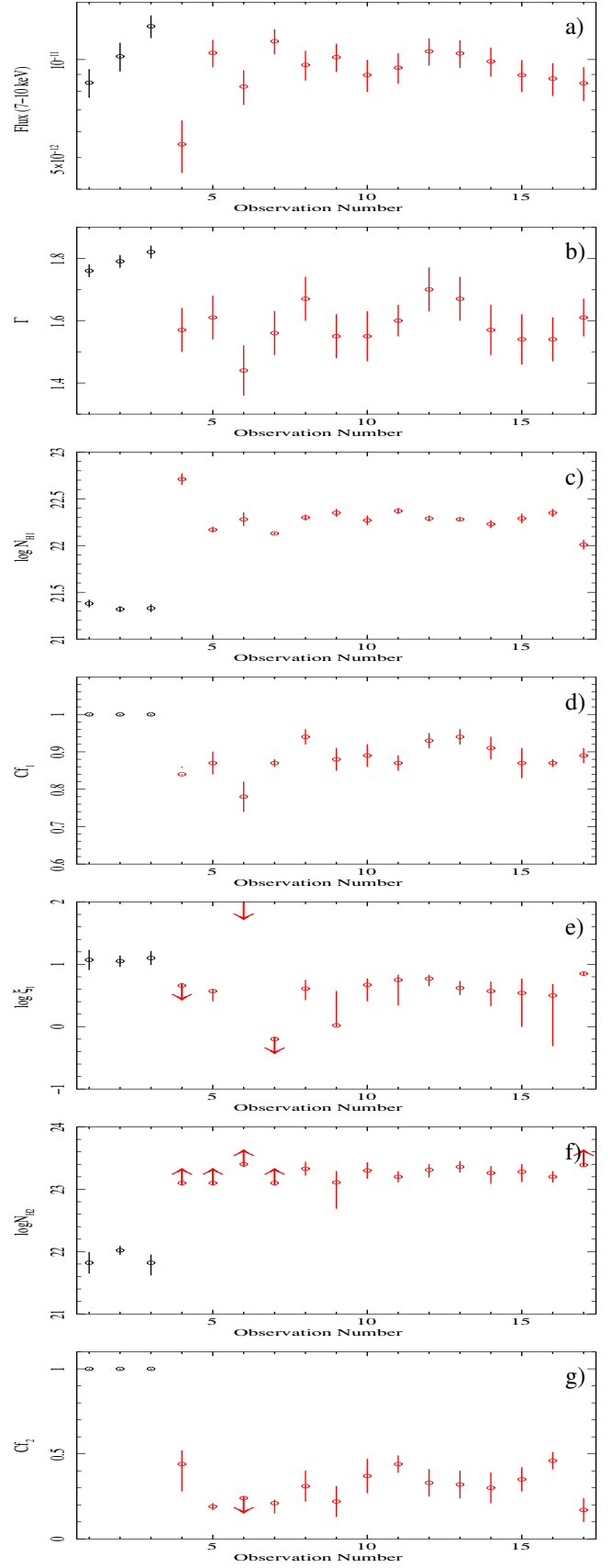
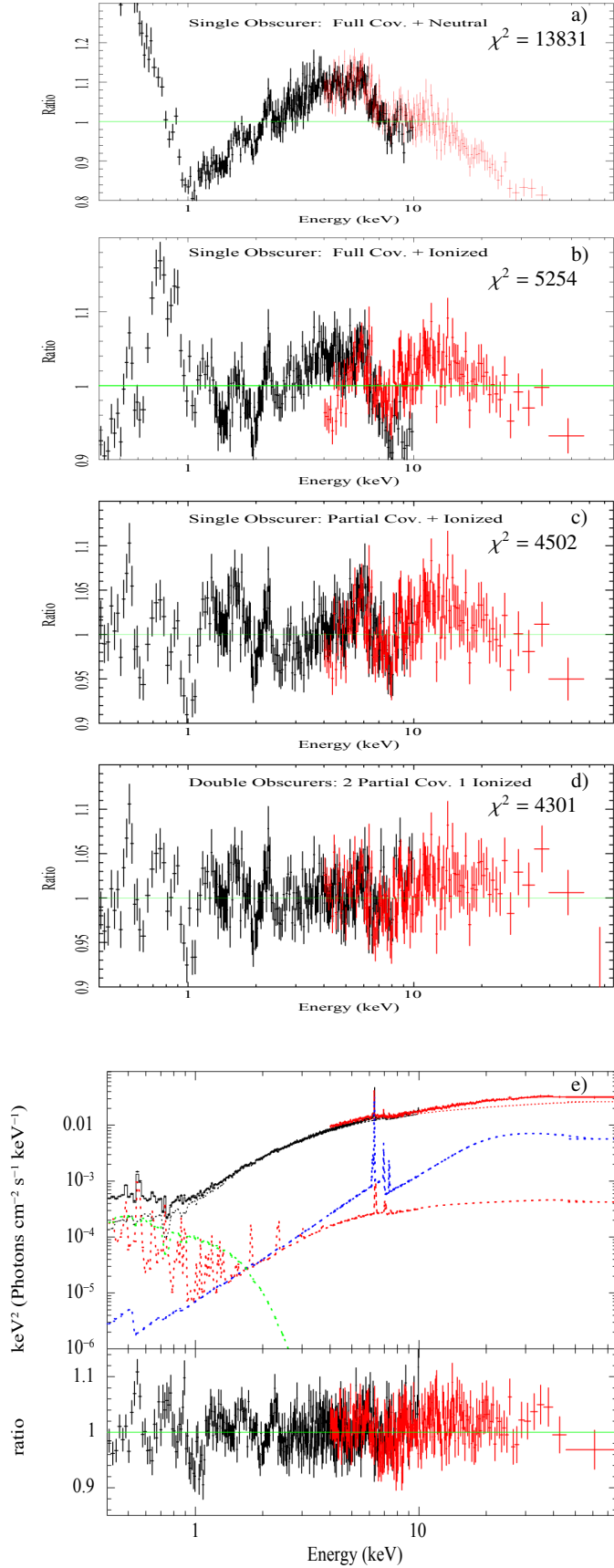


**Fig. 8.** Data-to-model ratios (panels a)–d) of the 3 *XMM-Newton*+*NuSTAR* observations for different models (see text for details) and plot of the unfolded best-fit spectrum of the grouped spectra (panel e).

**Fig. 9.** Interesting evolution of the spectral fit parameters versus the observation number (where, for better clarity, the archival observations are indicated in black, while those from the campaign are indicated in red). From *top to bottom*: power-law flux between 7–10 keV,  $\Gamma$ ,  $\log N_{\text{H1}}$ ,  $C_{f1}$ ,  $\log \xi_1$ ,  $\log N_{\text{H2}}$ , and  $C_{f2}$ , versus the observation number.

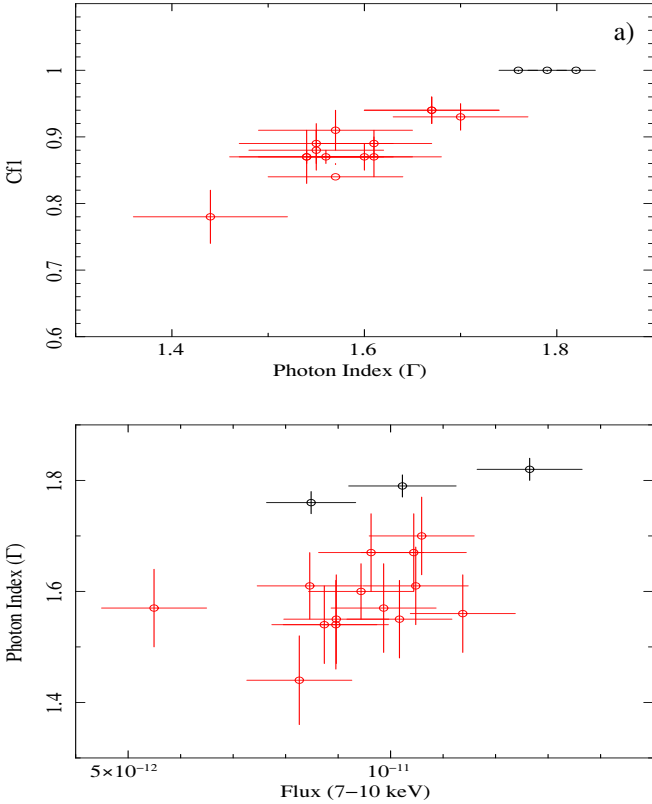


**Fig. 10.** (Panel **a**) Spectral fit parameters  $\Gamma$  versus  $C_{f_1}$  (panel **a**) and (panel **b**)  $\Gamma$  versus power law  $F_{7-10\text{ keV}}$  (panel **b**). Archival observations are indicated in black, while those from the campaign are indicated in red.

seen at lower energies can be ascribed to the obscurer itself, with only little changes in the intrinsic continuum flux and shape. This is confirmed in panels b to g of Fig. 9, which show the time variability of the most interesting best-fit parameters of the two obscurer(s) as a function of the observation number. This is also confirmed by our model-independent analysis and modeling of the fractional variability shown below. Overall, we find only weak (though statistically significant) variations of the ionization parameter  $\xi_1$ , while  $\xi_2$  is consistent with being  $\sim 0$  (i.e. neutral gas) since the start of the campaign, from observation M1. We note that, given the complexity of the multi-component spectral model used here, we did not find any single parameter that could be considered as being responsible, alone, for most of the observed spectral variability, but several parameters combined to produce the complex spectral variability shown below.

We then looked for trends and correlations among all the best-fit parameters listed in Fig. 9. We find only one weak, but significant, correlation between  $C_{f_1}$  and  $\Gamma$ , with  $C_{f_1} \approx 0.5 \times \Gamma + 0.1$  for a Pearson linear correlation coefficient of 0.94, corresponding to a chance probability of  $< 10^{-5}$  (see Fig. 10, panel a). The correlation also remains significant after deleting the three archival observations (correlation coefficient of 0.86, chance probability value of  $8 \times 10^{-5}$ ). Why would the covering factor, which is a geometrical factor, depend on the power-law intrinsic shape? This is certainly puzzling and will be addressed later in the discussion (Sect. 5.2). However, another possibility could be that the correlation is driven by an intrinsic degeneracy of the model parameters. A quantitative estimate of this effect would require extensive simulations involving complex models that are beyond the scope of this paper, but this caveat should be kept

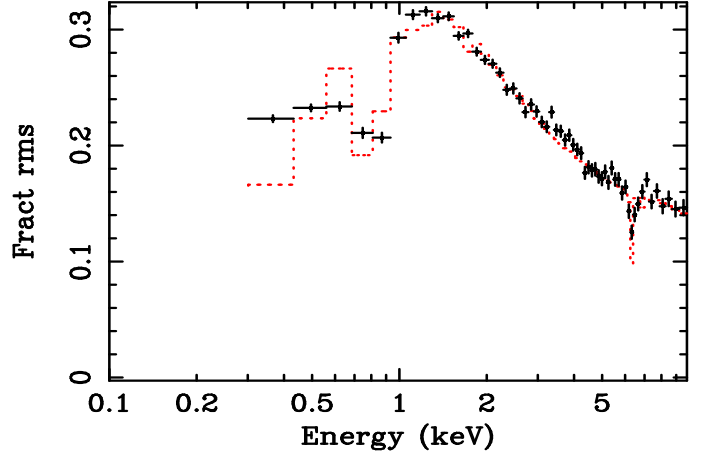


**Fig. 11.** Modelling of the  $F_{\text{var}}$  spectrum using best-fit model and best-fit parameters of Table 4.

in mind. Finally, a general trend (but not a correlation) is also found (see Fig. 10, panel b) where the source appears to be systematically intrinsically flatter during the (absorbed) campaign than during the archival (unabsorbed) observations. This point will also be briefly discussed in Sect. 5.2.

#### 4.4. Modeling of the XMM-Newton $F_{\text{var}}$ spectrum

We used the best fit spectral models during the campaign and described in Sect. 4.3.2 to derive the corresponding  $F_{\text{var}}$  spectra ( $F_{\text{var}}^{\text{model}}$  in the following), which we compared with the observed  $F_{\text{var}}$  spectrum of the campaign shown in Figs. 2 and 11 in an attempt to single out the main parameters responsible for the observed spectral variability.

We first checked whether our best-fit model can reproduce the  $F_{\text{var}}$  spectrum correctly by letting all the parameters of the model vary within the corresponding range of best-fit values listed in Table 4. The  $F_{\text{var}}^{\text{model}}$  curve is shown as a red dotted line in Fig. 11. The good agreement between the theoretical and the observed  $F_{\text{var}}$  demonstrates, as expected given the  $F_{\text{var}}$  calculation definition, that our best-fit spectral model is able to reproduce the correct flux variability at each energy. To obtain the  $F_{\text{var}}^{\text{model}}$  curve, the excess variance has been normalized by the total flux (which also includes the contribution from constant components) as a function of energy. This explains the net decrease of variability in the soft band and at  $\sim 6.4$  keV, where the constant soft scattered component (Sect. 4.2) and the narrow FeK emission line (Sect. 4.1.2) give significant contributions.

Figure 12 shows the theoretical  $F_{\text{var}}^{\text{model}}$  spectra obtained by varying just one parameter of the best-fit model (or a combination of parameters, normalization, and index, in the case of the power law) and leaving all the others fixed to the best-fit values of observation M7, chosen as a reference for its similarity to the average values. The variable parameter spans the 14 best-fit values listed in Table 4. These curves show the energy distribution of the variability power of the main parameters of the model. We note that the only components contributing to the soft band variability are the normalization of the intrinsic soft excess ( $A_{\text{comptt}}$ ), and the covering fraction of the mildly ionized obscurer ( $C_{f_1}$ ). On the other hand, the main parameters contributing to the variability above  $\sim 1$  keV are the column density of the mildly ionized obscurer,  $N_{\text{H1}}$ , and the power-law normalization and spectral index. Interestingly, the  $F_{\text{var}}$ , which was obtained by varying only the  $N_{\text{H1}}$  parameter, is characterized by a shape very similar to

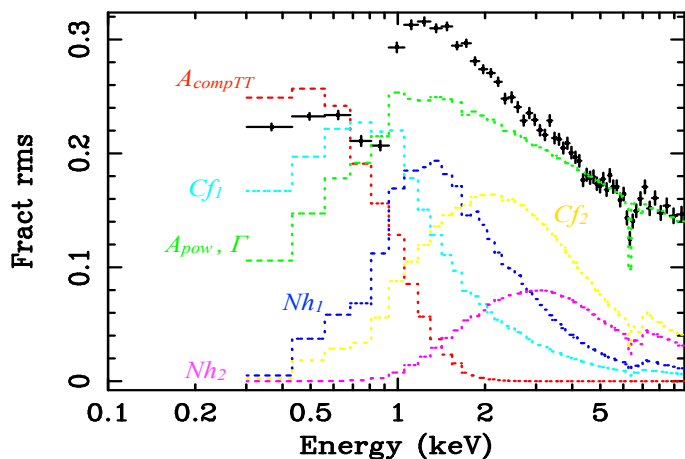


**Fig. 12.** Spectral decomposition of the different model components contributing to the total  $F_{\text{var}}$  spectrum.

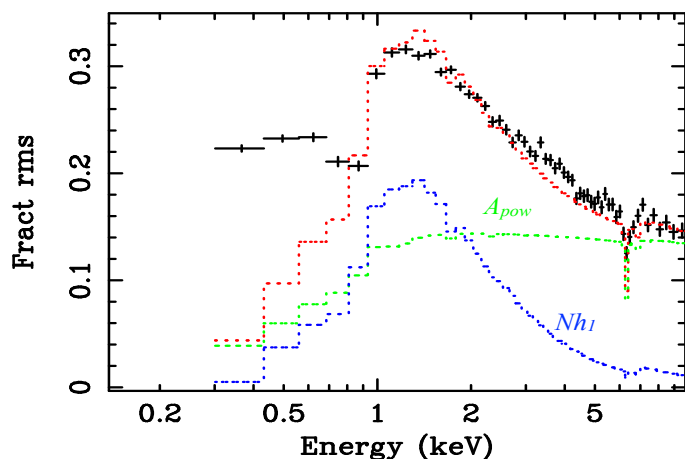


**Fig. 13.** Spectral decomposition varying only the column density of component 1 of the obscurer and the power-law normalization between 7–10 keV (see text for details).

the observed  $F_{\text{var}}$ , with a peak at 1–1.5 keV and a sharp drop in the soft band. We note also that the colder component of the obscurer ( $N_{\text{H}2}$  and  $C_{f2}$ ) brings only weak variability power, and mostly concentrated between 2–4 keV.

We verified whether variations of the  $N_{\text{H}1}$  parameter, plus variations of the normalization of the power law alone (i.e. without variation of  $\Gamma$ , the corresponding  $F_{\text{var}}$  being then constant over the entire energy range), can account for most of the observed variability above  $\sim 1$  keV. To this aim we combined the theoretical  $F_{\text{var}}$  curves obtained by varying the  $N_{\text{H}1}$  parameter only, and the power law flux in the energy range 7–10 keV (see Fig. 13). The 7–10 keV energy range was chosen (rather than the normalization at 1 keV, as given by XSPEC fits) so as to better constrain the intrinsic variations of the power-law normalization and avoid spurious contribution from other parameters (see Fig. 12). Figure 13 shows that most of the observed variability at  $E > 1$  keV can be explained by variations of  $N_{\text{H}1}$  and power-law normalization/flux. The residual variability in the soft band might be attributed either to the Comptt component and/or the covering fraction of the mildly ionized obscurer.

A similar model-independent analysis is presented in Paper VII for the whole *Swift* long-term monitoring, which probes typically longer timescales of variability than here, i.e. 10 days up to  $\sim 5$  months. For those periods, when the *Swift* monitoring

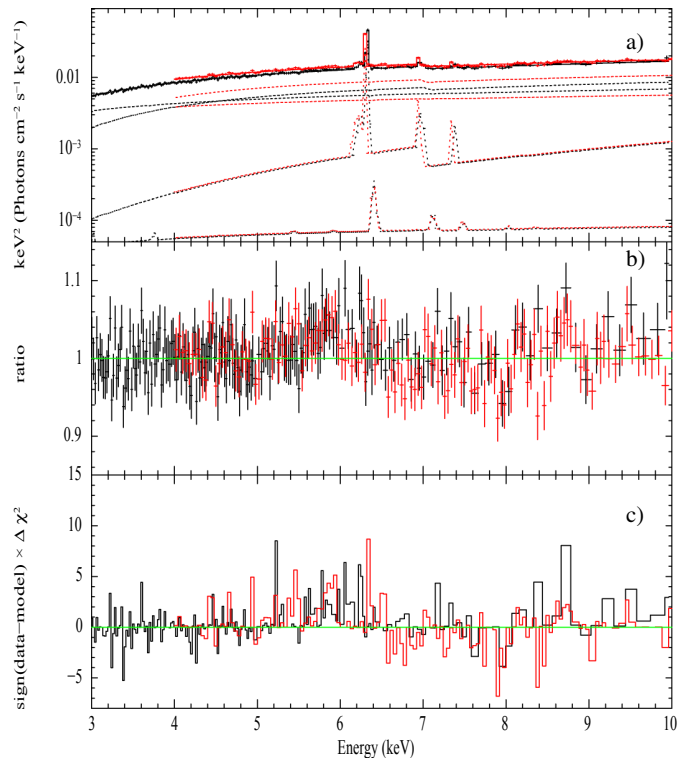


**Fig. 14.** The 3–10 keV band unfolded spectrum obtained from the spectra of the 3 *XMM-Newton* (black) + *NuSTAR* (in red) simultaneous observations. Spectra (panel a)), the data/model ratio (panel b)), and the residuals in units of  $\Delta\chi^2$  (panel c)).

included also the *XMM-Newton* campaign, the  $F_{\text{var}}$  recorded by *Swift* was consistent in shape with the *XMM-Newton* one, although with significantly lower statistical quality. *Swift* was not sensitive enough to constrain variations in column density, which was thus fixed at a constant value of  $1.2 \times 10^{22} \text{ cm}^{-2}$  as obtained from the time-averaged data presented in Paper 0, and most of the spectral variability was attributed to variations of the covering fraction of the obscurer only. Moreover, the signature of the  $N_{\text{H}1}$  variability, the very sharp “drop” below  $\sim 1$  keV in the pn  $F_{\text{var}}$  spectrum, was not apparent in the *Swift* data either. Given the lower S/N data and the longer timescales probed by *Swift*, we consider their results in agreement with the more detailed ones presented here.

#### 4.5. Additional emission and absorption complexities in the Fe K energy band

As mentioned above (Sect. 4.3), after reaching a best-fit broadband model of the 3 *XMM-Newton* + *NuSTAR* observations, we are still left with additional, albeit weak, features in the Fe K energy band, namely one moderately broad emission line feature below 6 keV, and a set of at least two absorption features, around 6.7–6.9 keV and  $\sim 8$  keV (see Fig. 14). As shown in Fig. 14, these features are seen in both pn (black) and *NuSTAR* (red), the latter having lower energy resolution but greater effective area than the pn at energies above 7–8 keV. The 6.7–6.9 keV feature was also detected in the MOS, while at higher energies the MOS statistics are not sufficient to either confirm or disprove the 8 keV line as well. The features are also seen, and at the same significance, if the background is not subtracted from the source+background spectra. F-tests indicate that both absorption lines are significant (at  $>99\%$ ), with  $\Delta\chi^2 \sim 25\text{--}30$

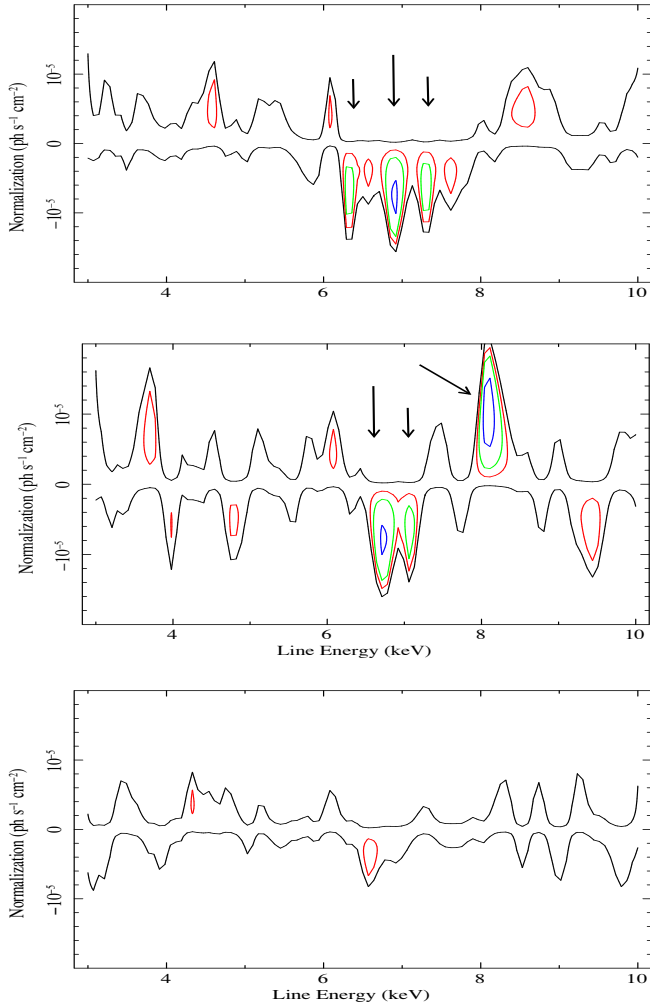


**Fig. 15.** Three examples of confidence contours ( $\Delta\chi^2 = +0.5, -2.3, -4.61,$  and  $-9.21$  for the black, red, green, and blue contours, respectively) of energy vs. intensity of a narrow emission/absorption line between 3–10 keV during observations M2 (*top panel*), M10 (*middle panel*), and M3 (*bottom panel*). These illustrate the typical intensity of residuals left in the observation-by-observation best-fit spectra around 6–8 keV with (*top and middle panels*) and without residuals left (*bottom panel*).

and  $EW \sim 15\text{--}20$  eV, each. A careful investigation of these features in the other 14 single *XMM-Newton* observations indicates, however, that none of them remains always significant during the campaign. Absorption features between 6.4–7.1 keV are seen in  $\sim 10$  out of the 17 observations, while the emission below 6 keV and the feature around 8 keV are seen only in a handful of observations. In all cases, their EWs and statistical significance are low, typically  $\lesssim 20$  eV and  $\Delta\chi^2$  between 3 and 10, each. To illustrate further these remaining features, three examples of residuals obtained during observations M2, M10, and M3 are shown in Fig. 15, where confidence contours ( $\Delta\chi^2 = +0.5, -2.3, -4.61,$  and  $-9.21$  for the black, red, green, and blue contours, respectively) are shown for a narrow emission/absorption feature “scanned” through the best-fit spectra.

There could be several different explanations for these remaining weak features, including either a wrong, or incomplete, modeling of the complex underlying continuum which includes several emission lines in the FeK band from both the reflection and scattered components, or some weak contribution from the

pn background, which has some strong emission lines at high energies. Another obvious explanation could be the presence of an additional outflowing absorption component, at such a high ionization state to contribute only/mostly with FeXXV ( $\text{He-}\alpha$  and  $\text{He-}\beta$ ) and FeXXVI ( $\text{Ly-}\alpha$  and  $\text{Ly-}\beta$ ) absorption lines. Alternatively, both these remaining blueshifted absorption features and red-shifted emission features could be signatures of a Fe P-Cygni type emission and absorption profile originating in an outflowing, highly ionized wind (Dorodnitsyn 2010; Hagino et al. 2015; Gardner & Done 2015; Nardini et al. 2015). Finally, another possibility for the 6 keV emission line could be a (yet unmodelled) contribution from a weak, and significantly redshifted and broadened reflection component. Overall, given the weakness and marginal statistical significance of any of these additional emission and absorption complexities, we refrain here from attempting to model them with either a proper physical wind model (which would include the expected P-Cygni FeK line profile) or a relativistically blurred reflection model, since these would go beyond the scope of this paper and the quality of these datasets.

## 5. Discussion

### 5.1. On the origin of the reflector

A first estimate on the location of the Fe K emitting region can be obtained directly from the measured line width of the Fe  $K\alpha$  emission line. After proper correction for the pn CTI (which produced both energy shift and broadening of the line, see Sect. 2), we obtain an upper-limit of  $2340 \text{ km s}^{-1}$  on the line width, namely  $v_{\text{FWHM}} \lesssim 5500 \text{ km s}^{-1}$ . Thus, assuming Keplerian motion,  $R \sim GM_{\text{BH}}/v^2$ , where we define the velocity width as  $\frac{v=\sqrt{3}}{2} v_{\text{FWHM}}$ . For an estimated black hole mass of NGC 5548 of  $M_{\text{BH}} \sim 3.24 \times 10^7 M_{\odot}$  (Pancoast et al. 2015), this corresponds to  $R > 1.89 \times 10^{16} \text{ cm}$  (0.006 pc, or light days). We note that this limit is consistent with the upper values in the velocity found for the UV broad absorption line components (Paper 0), consistent with a possible common origin.

The limits obtained from the lack of variability of the line intensity, despite some weak, but significant variability in the 7–10 keV illuminating component, place even stronger constraints on the minimum distance of the Fe K reflector from the source. We note that the model-independent  $F_{\text{var}}$  spectrum clearly shows weaker line variability, compared to the underlying continuum variability, indicating that the FeK line does not follow the underlying continuum variations on timescales as long as  $\sim$ months. This would thus imply a production site greater than a  $\sim$ months light-scale (i.e.  $\geq 0.026$  pc), although a detailed estimate of its distance would also depend on the exact reflector geometry and on the source light-curve history, which are both unknown. This is nevertheless also consistent with the only other finding of variability of the FeK line in NGC 5548, which indicated in long RXTE monitoring observations a weak but significant correlation on long (months to years) timescales between the FeK line flux and the continuum intensity (Markowitz et al. 2003). This is also consistent with the limits placed by Liu et al. (2010), based on the lack of variability of the FeK line during a  $\sim 50$  days monitoring with the *Suzaku* satellite performed in 2007.

### 5.2. On the origin of the obscurer

We attempt to put constraints on the location and the physical origin of the obscurer, based on its observed ionization state and

variability properties. In agreement with, and extending previous results (Papers III and VII), the present analysis (Sects. 4.3 and 4.4) provides evidence that most of the spectral variability can be explained by changes in column density (and, to a lesser extent, covering factor) occurring along the LOS and, owing to transverse motions of gas across the emission region, on top of a power law that is weakly variable in intensity and shape.

Assuming that the obscuring cloud(s) follow(s) a Keplerian orbit, given the measured ionization state and the variability timescale and amplitude of the absorption variations, we can estimate a rough location of the obscurer by using Eq. (8) in Svoboda et al. (2015) (analogous to Eq. (3) in Lamer et al. 2003). Given the BH mass in NGC 5548 of  $3.24 \times 10^7 M_{\odot}$ , the average ionizing luminosity between 13.6 eV and 13.6 keV of  $\approx 8.6 \times 10^{43}$  erg/s during the campaign, the sampled minimum timescale of  $\sim 2$  days, over which we find a significant change of column density ( $\Delta \log N_{\text{HI}} \approx 21.7 \text{ cm}^{-2}$ ), and the ionization parameter  $\log \xi \sim 0.6 \text{ erg cm}^{-2} \text{ s}$ , we obtain a rough estimate of the distance of the obscuring cloud(s) of  $R \approx 3 \times 10^{17} \text{ cm} \approx 0.1 \text{ pc} \approx 116$  light days. Despite being recorded here for the first time in this source, this kind of “obscuration event” may not be unique to NGC 5548. Albeit with less quality data, other fast and variable obscuration events have been recorded in the past in a number of intermediate-type or type 1 sources, such as NGC 3227 (Lamer et al. 2003), NGC 1365 (Risaliti et al. 2005), NGC 4388 (Elvis et al. 2004), NGC 4151 (Puccetti et al. 2007), PG1535+547 (Ballo et al. 2008), NGC 7582 (Bianchi et al. 2009), H0557-385 (Longinotti et al. 2009; Coffey et al. 2014), Mrk 766 (Risaliti et al. 2011), SwiftJ2127.4+5654 (Sanfrutos et al. 2013), Mrk 335 (Longinotti et al. 2013), NGC 5506 (Markowitz et al. 2014), NGC 985 (Ebrero et al. 2016a,b), Fairall 51 (Svoboda et al. 2015), and ESO 323-G77 (Sanfrutos et al. 2016), not to mention the systematic surveys by Malizia et al. (1997), Markowitz et al. (2014), and Torricelli-Ciamponi et al. (2015). Based on various arguments, such as the ones above, and including the spectral properties and variability timescales of the absorbers, most authors have associated the origin of the absorbing clouds as either broad line region (BLR) clouds, a clumpy torus, or the inner boundary of a dusty torus. However there is no proof yet that the clouds probed in X-rays are actually in an orbital Keplerian equilibrium, as usually assumed, and there is no clear explanation yet on what the physical origin for the structure and dynamics of the BLR clouds is either. In fact, the clouds detected in X-rays, and possibly also the BLR clouds, could both be facets of the same phenomenon, namely a large-scale accretion disc outflow (see e.g. Emmering et al. 1992; Elitzur & Ho 2009; Takeuchi et al. 2013; Waters et al. 2016).

The uniqueness of our findings for NGC 5548 is that they support an origin of the obscurer, as being part of (or within) such an outflowing accretion disc wind, and where the BLR could possibly be identified with the virialized and terminal part of it. The evidences in support of this hypothesis are that (i) simultaneously to the above X-ray obscurer measurement, clear and strong UV broad (up to  $\sim 5000 \text{ km s}^{-1}$ ) absorption lines were detected for the first time in this source (Papers 0 and I); (ii) the obscuration event, despite being variable in time, down to a few days timescale, has remained systematically present since  $\sim$ year 2012, i.e. for the last four years (as shown by the analysis of the *Swift* long-term light curves, Paper VII), and it is still present at the end of year 2015 (Kriss et al., in prep.); (iii) detailed modeling of the BLR in NGC 5548 (Pancoast et al. 2014) constrains the inclination of our viewing angle to NGC 5548 to a very low value of  $30 \pm 1$  deg, i.e. almost face on, which makes any equatorial-only geometrical configuration (such as with the

BLR or torus structures) difficult to reconcile with this data. This would instead favor more polarly directed components such as those found in MHD-driven outflows (Blandford & Payne 1982; Fukumura et al. 2014), or vertically expanded super-critical outflows (Takeuchi et al. 2013), although this source definitely is not a super-critical system.

Intriguingly, we find no particular property of the source during our multi-frequency campaign that could help us understand the origin and reason for the onset of this long-lasting obscuration event. For example, the measured luminosities at UV, soft, and hard X-rays are absolutely in line with historical values for this source. The only unusual property that we found is that the photon index of the underlying power law appears to be systematically and significantly flatter compared to historical values ( $\Gamma \sim 1.7\text{--}1.9$ ) for this source, even considering only the data above 7 keV, where the effect of any residual absorption left should be negligible. This may be indicative of a particular ionization state, or physical phenomenon, that favors the formation of an outflow from the accretion disc. The apparent state-dependence of winds in Galactic binaries, where they seem to be preferentially detected when in their (steeper) high-soft state (e.g. Ponti et al. 2012b), would suggest that this is not the case though.

We also find a significant correlation between  $C_{f_1}$  and the photon index  $\Gamma$  (Sect. 4.3.2 and Fig. 10), which would be puzzling if not related to remaining parameter degeneracies in the fit procedure. Still, to try to explain it, one possibility could be that we are witnessing changes in the corona geometry that are linked to its cooling rate, and/or vice-versa. For example, assuming a disk-corona geometry similar to the one assumed for Mrk 509 (Petrucci et al. 2013), with an outer accretion disk and an inner corona (within  $r_{\text{cor}}$ ). An increase of  $\dot{M}_{\text{acc}}$  could plausibly produce a decrease of  $r_{\text{cor}}$  (due to, for example disk recondensation, e.g. Meyer-Hofmeister & Meyer 2006), thereby reducing the size of the corona, and thus increasing the effective Cf of the obscurer. At the same time, the higher  $\dot{M}_{\text{acc}}$  would also increase the source UV flux, producing an increase of cooling in the X-ray corona, and then a softening of the X-ray spectrum. This would also be consistent with the “softer when brighter” behavior of this source, as previously found in Papers III and VII. In turn, the higher  $\dot{M}_{\text{acc}}$  would also explain the higher outflow rate, as expected for most disc-wind models (Elitzur & Ho 2009; Nicastro 2000), and predicts that the width of the BLR becomes narrower with respect to historical measurements (Nicastro 2000).

## 6. Conclusions

The *XMM-Newton* monitoring campaign performed in the summer of 2013 revealed NGC 5548 in a heavily obscured state (Paper 0). This obscuration was unexpected because this source, often taken as an example of a prototypical Seyfert 1 galaxy, had never been found in a strongly absorbed state within the last 40–50 years of observations (Paper VI).

Here we have focused on the analysis of the EPIC pn data, which clearly shows the obscuration of the X-ray spectra and the three archival *XMM-Newton* observations, and we have also combined the simultaneous *NuSTAR* data that were available during three of the 17 *XMM-Newton* observations. Very importantly for our analysis, we took advantage of our previous papers on this campaign, i.e. Papers 0 to VII, to obtain a best-fit model that is consistent and physically well motivated, taking into account all available information from the many datasets of the campaign (including RGS data, *Swift*, and HST/COS).

The main results of our spectral analysis are as follows:

- A best-fit is found, first based on the three *XMM-Newton* + *NuSTAR* observations, and then applied to all 17 *XMM-Newton* observations, which includes: (i) a power law continuum with  $\Gamma \sim 1.5\text{--}1.7$ ; (ii) a cold and constant reflection component that produces a narrow Fe K emission line plus Compton hump; (iii) a soft-excess modeled by thermal Comptonization and contributing only below  $\sim 1$  keV; (iv) a scattered emission line component dominating the RGS energy band; (v) a constant, multi temperature warm absorber, consistent with its historical values, after accounting for deionization owing to the obscurer itself; and (vi) a multilayer obscurer at mild-to-neutral ionization state, and with at least two components, which partially cover the source. This obscurer is in addition to the multicomponent warm absorber that is always present in this source (Paper VI).
- The Fe K line properties (energy, width, equivalent width, and intensity) are consistent with being part of a reflection component that is produced by a cold reflecting medium located at distances greater than  $\sim 0.006$  pc ( $\sim 7$  light days) from the source.
- The intrinsic high-energy continuum did not vary strongly (neither in flux nor in shape) during the observations, implying that most of the soft X-ray variations can be ascribed to changes in the properties of the new obscurer(s) found along the LOS to NGC 5548.
- The curvature of the continuum at lower energies and its variability clearly requires a complex and intrinsically variable multi-layer absorber. From the analysis of the spectral variability, we find a satisfactory explanation in terms of variability of mostly its column density and, to a lesser extent, covering factor.
- Consistent with previous results, the picture that has emerged suggests the presence of a large-scale/elongated (persistent over years) but inhomogeneous absorbing structure that appears along the LOS of NGC 5548. We argue that the full (multi-frequency and multi-epoch) data favor an origin in an accretion disc wind.
- Unfortunately, we could not constrain the velocity of the X-ray obscurer directly from the X-ray data, but its appearance simultaneous to the UV broad absorption lines (with  $v$  up to  $\sim 5000$  km s $^{-1}$ ) makes a strong case in favor of a direct physical association between the two, which is coherent with Paper 0.

Finally, we have also shown (Sect. 4.5) marginal evidence for additional emission and absorption features around the FeK energy band, indicating further complexities in either the reflecting or absorbing media in this source. These could be related to an additional outflowing component, potentially at an even higher ionization state and velocity than measured here. Given the little statistical significance of these features, summed to the complexity of the multiple component model and to the calibration uncertainties of the present dataset, we have not discussed these to a great extent. Overall, these observations and theoretical models have reached a level at which we are really pushing the limits of the calibration uncertainties, which are hard to resolve. Certainly, a better understanding of the obscurer origin and properties would benefit from more sensitive and higher energy resolution, as foreseen with the future Athena Space Observatory.

*Acknowledgements.* This paper is based on observations obtained with the *XMM-Newton* satellite, an ESA funded mission with contributions by ESA Member States and USA. M.C. and S.B. acknowledges financial support from the Italian Space Agency under grant ASI-INAF I/037/12/P1. G.P. acknowledges

support via an EU Marie Curie Intra-European fellowship under contract no. FP-PEOPLE-2012-IEF-331095. This work is based on observations obtained with *XMM-Newton*, an ESA science mission with instruments and contributions directly funded by ESA Member States and the USA (NASA). This research has made use of data obtained with the *NuSTAR* mission, a project led by the California Institute of Technology (Caltech), managed by the Jet Propulsion Laboratory (JPL) and funded by NASA. We thank the International Space Science Institute (ISSI) in Bern for their support and hospitality. SRON is supported financially by NWO, the Netherlands Organization for Scientific Research. M.M. acknowledges support from NWO and the UK STFC. This work was supported by NASA through grants for HST program number 13184 from the Space Telescope Science Institute, which is operated by the Association of Universities for Research in Astronomy, incorporated under NASA contract NAS5-26555. M.C. acknowledges financial support from contracts ASI/INAF n.I/037/12/0 and PRIN INAF 2011 and 2012. P.-O.P. acknowledges financial support from the CNES and from the CNRS/PICS. K.C.S. acknowledges financial support from the Fondo Fortalecimiento de la Productividad Científica VRIDT 2013. E.B. received funding from the EU Horizon 2020 research and innovation programme under the Marie Skłodowska-Curie grant agreement No. 655324, and from the iCORE program of the Planning and Budgeting Committee (grant No. 1937/12). S.B., G.M., and A.D.R. acknowledge INAF/PICS financial support. G.M. and F.U. acknowledge financial support from the Italian Space Agency under grant ASI/INAF I/037/12/0-011/13. B.M.P. acknowledges support from the US NSF through grant AST-1008882. G.P. acknowledges support via an EU Marie Curie Intra-European fellowship under contract No. FP-PEOPLE-2012-IEF-331095 and Bundesministerium für Wirtschaft und Technologie/Deutsches Zentrum für Luft- und Raumfahrt (BMW/DLR, FKZ 50 OR 1408). F.U. acknowledges Ph.D. funding from the VINCI program of the French-Italian University. M.W. acknowledges the support of a Ph.D. studentship awarded by the UK STFC.

## References

- Andrade-Velázquez, M., Krongold, Y., Elvis, M., et al. 2010, *ApJ*, **711**, 888
- Antonucci, R. R. J., & Miller, J. S. 1985, *ApJ*, **297**, 621
- Arav, N., Chamberlain, C., Kriss, G. A., et al. 2015, *A&A*, **577**, A37 (Paper II)
- Ballo, L., Giustini, M., Scharrel, N., et al. 2008, *A&A*, **483**, 137
- Bassani, L., Dadina, M., Maiolino, R., et al. 1999, *ApJS*, **121**, 473
- Behar, E., Sako, M., & Kahn, S. M. 2001, *ApJ*, **563**, 497
- Bianchi, S., Piconcelli, E., Chiaberge, M., et al. 2009, *ApJ*, **695**, 781
- Blandford, R. D., & Payne, D. G. 1982, *MNRAS*, **199**, 883
- Blustin, A. J., Page, M. J., Fuerst, S. V., Branduardi-Raymont, G., & Ashton, C. E. 2005, *A&A*, **431**, 111
- Brenneman, L. W., Elvis, M., Krongold, Y., Liu, Y., & Mathur, S. 2012, *ApJ*, **744**, 13
- Cappi, M. 2006, *Astron. Nachr.*, **327**, 1012
- Cappi, M., Panessa, F., Bassani, L., et al. 2006, *A&A*, **446**, 459
- Coffey, D., Longinotti, A. L., Rodríguez-Ardila, A., et al. 2014, *MNRAS*, **443**, 1788
- Cooke, B. A., Ricketts, M. J., Maccacaro, T., et al. 1978, *MNRAS*, **182**, 489
- Costantini, E. 2010, *Space Sci. Rev.*, **157**, 265
- Crenshaw, D. M., Kraemer, S. B., & George, I. M. 2003a, *ARA&A*, **41**, 117
- Crenshaw, D. M., Kraemer, S. B., Gabel, J. R., et al. 2003b, *ApJ*, **594**, 116
- Dadina, M. 2007, *A&A*, **461**, 1209
- de la Calle, I. 2014, Users Guide to the *XMM-Newton* Science Analysis System, Issue 11.0 (ESA: *XMM-Newton* SOC)
- Dickey, J. M., & Lockman, F. J. 1990, *ARA&A*, **28**, 215
- Di Gesu, L., Costantini, E., Ebrero, J., et al. 2015, *A&A*, **579**, A42 (Paper IV)
- Dorodnitsyn, A. V. 2010, *MNRAS*, **406**, 1060
- Ebrero, J., Kriss, G. A., Kaastra, J. S., & Ely, J. C. 2016a, *A&A*, **586**, A72
- Ebrero, J., Kaastra, J. S., Kriss, G. A., et al. 2016b, *A&A*, **587**, A129 (Paper VI)
- Elitzur, M., & Ho, L. C. 2009, *ApJ*, **701**, L91
- Elitzur, M., & Shlosman, I. 2006, *ApJ*, **648**, L101
- Elvis, M. 2000, *ApJ*, **545**, 63
- Elvis, M., Risaliti, G., Nicastro, F., et al. 2004, *ApJ*, **615**, L25
- Emmering, R. T., Blandford, R. D., & Shlosman, I. 1992, *ApJ*, **385**, 460
- Ferland, G. J., Porter, R. L., van Hoof, P. A. M., et al. 2013, *Rev. Mex. Astron. Astrofís.*, **49**, 137
- Fukumura, K., Tombesi, F., Kazanas, D., et al. 2014, *ApJ*, **780**, 120
- Ganguly, R., & Brotherton, M. S. 2008, *ApJ*, **672**, 102
- Gardner, E., & Done, C. 2015, *MNRAS*, **448**, 2245
- Gofford, J., Reeves, J. N., Tombesi, F., et al. 2013, *MNRAS*, **430**, 60
- Guainazzi, M., on behalf of the EPIC consortium, 2014, *XMM-Newton* Calibration Technical Note, XMM-SOC-CAL-TN-0018 (ESA: *XMM-Newton* SOC)
- Hagino, K., Odaka, H., Done, C., et al. 2015, *MNRAS*, **446**, 663
- Hoening, S. F. 2013, ArXiv e-prints [arXiv:1301.1349]

- Kaastra, J. S., & Barr, P. 1989, *A&A*, **226**, 59
- Kaastra, J. S., Mewe, R., Liedahl, D. A., Komossa, S., & Brinkman, A. C. 2000, *A&A*, **354**, L83
- Kaastra, J. S., Steenbrugge, K. C., Raassen, A. J. J., et al. 2002, *A&A*, **386**, 427
- Kaastra, J. S., Steenbrugge, K. C., Crenshaw, D. M., et al. 2004, *A&A*, **422**, 97
- Kaastra, J. S., Kriss, G. A., Cappi, M., et al. 2014, *Science*, **345**, 64 (Paper 0)
- Krolik, J. H., & Begelman, M. C. 1988, *ApJ*, **329**, 702
- Krongold, Y., Elvis, M., Andrade-Velazquez, M., et al. 2010, *ApJ*, **710**, 360
- Liu, Y., Elvis, M., McHardy, I. M., et al. 2010, *ApJ*, **710**, 1228
- Lamer, G., Uttley, P., & McHardy, I. M. 2003, *MNRAS*, **342**, L41
- Lobban, A. P., Reeves, J. N., Miller, L., et al. 2011, *MNRAS*, **414**, 1965
- Lodders, K. 2003, *ApJ*, **591**, 1220
- Longinotti, A. L., Bianchi, S., Ballo, L., de La Calle, I., & Guainazzi, M. 2009, *MNRAS*, **394**, L1
- Longinotti, A. L., Krongold, Y., Kriss, G. A., et al. 2013, *ApJ*, **766**, 104
- Madsen, K. K., Fürst, F., Walton, D. J., et al. 2015, *ApJ*, **812**, 14
- Malizia, A., Bassani, L., Stephen, J. B., Malaguti, G., & Palumbo, G. G. C. 1997, *ApJS*, **113**, 311
- Marchese, E., Braitto, V., Della Ceca, R., Caccianiga, A., & Severgnini, P. 2012, *MNRAS*, **421**, 1803
- Markowitz, A., Edelson, R., & Vaughan, S. 2003, *ApJ*, **598**, 935
- Markowitz, A. G., Krumpe, M., & Nikutta, R. 2014, *MNRAS*, **439**, 1403
- McHardy, I. M., Cameron, D. T., Dwelly, T., et al. 2014, *MNRAS*, **444**, 1469
- Mehdipour, M., Branduardi-Raymont, G., Kaastra, J. S., et al. 2011, *A&A*, **534**, A39
- Mehdipour, M., Kaastra, J. S., Kriss, G. A., et al. 2015, *A&A*, **575**, A22 (Paper I)
- Mehdipour, M., Kaastra, J. S., Kriss, G. A., et al. 2016, *A&A*, **588**, A139 (Paper VII)
- Merloni, A., Bongiorno, A., Brusa, M., et al. 2014, *MNRAS*, **437**, 3550
- McKernan, B., Yaqoob, T., & Reynolds, C. S. 2007, *MNRAS*, **379**, 1359
- Meyer-Hofmeister, E., & Meyer, F. 2006, *A&A*, **449**, 443
- Miller, L., Turner, T. J., Reeves, J. N., et al. 2007, *A&A*, **463**, 131
- Miniutti, G., Sanfrutos, M., Beuchert, T., et al. 2014, *MNRAS*, **437**, 1776
- Murray, N., Chiang, J., Grossman, S. A., & Voit, G. M. 1995, *ApJ*, **451**, 498
- Nandra, K., George, I. M., Mushotzky, R. F., Turner, T. J., & Yaqoob, T. 1997, *ApJ*, **476**, 70
- Nandra, K., O'Neill, P. M., George, I. M., & Reeves, J. N. 2007, *MNRAS*, **382**, 194
- Nardini, E., Reeves, J. N., Gofford, J., et al. 2015, *Science*, **347**, 860
- Nicastro, F. 2000, *ApJ*, **530**, L65
- Pancoast, A., Brewer, B. J., Treu, T., et al. 2014, *MNRAS*, **445**, 3073
- Pancoast, A., Brewer, B. J., Treu, T., et al. 2015, *MNRAS*, **448**, 3070
- Panessa, F., Bassani, L., Cappi, M., et al. 2006, *A&A*, **455**, 173
- Piconcelli, E., Jimenez-Bailón, E., Guainazzi, M., et al. 2005, *A&A*, **432**, 15
- Petrucchi, P.-O., Paltani, S., Malzac, J., et al. 2013, *A&A*, **549**, A73
- Ponti, G. 2007, Ph.D. Thesis, University of Bologna, Italy
- Ponti, G., Cappi, M., Dadina, M., & Malaguti, G. 2004, *A&A*, **417**, 451
- Ponti, G., Papadakis, I., Bianchi, S., et al. 2012a, *A&A*, **542**, A83
- Ponti, G., Fender, R. P., Begelman, M. C., et al. 2012b, *MNRAS*, **422**, 11
- Pounds, K. A., Reeves, J. N., King, A. R., et al. 2003a, *MNRAS*, **345**, 705
- Pounds, K. A., Reeves, J. N., Page, K. L., et al. 2003b, *MNRAS*, **341**, 953
- Pounds, K. A., Reeves, J. N., Page, K. L., & O'Brien, P. T. 2004, *ApJ*, **616**, 696
- Proga, D. 2007, *ApJ*, **661**, 693
- Puccetti, S., Fiore, F., Risaliti, G., et al. 2007, *MNRAS*, **377**, 607
- Risaliti, G., Elvis, M., & Nicastro, F. 2002, *ApJ*, **571**, 234
- Risaliti, G., Bianchi, S., Matt, G., et al. 2005, *ApJ*, **630**, L129
- Risaliti, G., Salvati, M., Elvis, M., et al. 2009, *MNRAS*, **393**, L1
- Risaliti, G., Elvis, M., Bianchi, S., & Matt, G. 2010, *MNRAS*, **406**, L20
- Risaliti, G., Nardini, E., Salvati, M., et al. 2011, *MNRAS*, **410**, 1027
- Rivers, E., Risaliti, G., Walton, D. J., et al. 2015, *ApJ*, **804**, 107
- Reeves, J. N., Porquet, D., Braitto, V., et al. 2013, *ApJ*, **776**, 99
- Reeves, J. N., Braitto, V., Gofford, J., et al. 2014, *ApJ*, **780**, 45
- Sanfrutos, M., Miniutti, G., Agís-González, B., et al. 2013, *MNRAS*, **436**, 1588
- Sanfrutos, M., Miniutti, G., Krongold, Y., Agís-González, B., & Longinotti, A. L. 2016, *MNRAS*, **457**, 510
- Sim, S. A., Long, K. S., Miller, L., & Turner, T. J. 2008, *MNRAS*, **388**, 611
- Smith, M. J. S., Stuhlinger, M., Saxton, R. D., & Freyberg, M. J. 2014, *XMM-Newton* CCF Release Note, XMM-CCF-REL-323 (ESA: XMM-Newton SOC)
- Steenbrugge, K. C., Kaastra, J. S., de Vries, C. P., & Edelson, R. 2003, *A&A*, **402**, 477
- Steenbrugge, K. C., Kaastra, J. S., Crenshaw, D. M., et al. 2005, *A&A*, **434**, 569
- Svoboda, J., Beuchert, T., Guainazzi, M., et al. 2015, *A&A*, **578**, A96
- Takeuchi, S., Ohsuga, K., & Mineshige, S. 2013, *PASJ*, **65**,
- Tatum, M. M., Turner, T. J., Miller, L., & Reeves, J. N. 2013, *ApJ*, **762**, 80
- Tombesi, F., Cappi, M., Reeves, J. N., et al. 2010, *A&A*, **521**, A57
- Tombesi, F., Cappi, M., Reeves, J. N., et al. 2013, *MNRAS*, **430**, 1102
- Tombesi, F., Tazaki, F., Mushotzky, R. F., et al. 2014, *MNRAS*, **443**, 2154
- Torricelli-Ciamponi, G., Pietrini, P., Risaliti, G., & Salvati, M. 2014, *MNRAS*, **442**, 2116
- Turner, T. J., George, I. M., Nandra, K., & Mushotzky, R. F. 1997, *ApJ*, **488**, 164
- Turner, T. J., George, I. M., Nandra, K., & Mushotzky, R. F. 1998, *ApJ*, **493**, 91
- Turner, T. J., Miller, L., Kraemer, S. B., Reeves, J. N., & Pounds, K. A. 2009, *ApJ*, **698**, 99
- Ursini, F., Boissay, R., Petrucci, P.-O., et al. 2015, *A&A*, **577**, A38 (Paper III)
- Uttley, P., McHardy, I. M., & Papadakis, I. E. 2002, *MNRAS*, **332**, 231
- Vaughan, S., Edelson, R., Warwick, R. S., & Uttley, P. 2003, *MNRAS*, **345**, 1271
- Walton, D. J., Risaliti, G., Harrison, F. A., et al. 2014, *ApJ*, **788**, 76
- Waters, T., Kashi, A., Proga, D., et al. 2016, *ApJ*, submitted [arXiv:1601.05181]
- Whewell, M., Branduardi-Raymont, G., Kaastra, J. S., et al. 2015, *A&A*, **581**, A79 (Paper V)